ABSTRACT

Risk assessment of CO_2 storage requires the use of geophysical monitoring techniques to quantify changes in selected reservoir properties such as CO_2 saturation, pore pressure and porosity. Conformance monitoring and associated decision-making rest upon the quantified properties derived from geophysical data. It is consequently crucial that these properties are estimated with uncertainty assessment. A general framework combining seismic and controlled source electromagnetic (CSEM) inversion in a first step, with rock physics inversion in a second step is proposed. Fully Bayesian formulations are used in both steps allowing proper quantification of uncertainty. The Bayesian rock physics inversion is the main focus and rests upon two stages. The first one is a search stage and consists in exploring the model space and deriving models with associated probability density function (PDF). The second one is an appraisal or importance sampling stage, which is used as a "correction" step to ensure that the full model space is explored and that the estimated posterior PDF can be used to derive quantities like marginal probability densities. Both steps are based on the neighbourhood algorithm. The approach does not require any linearization of the rock physics model or assumption about the model parameters distribution. After describing the CO_2 storage context, the available data at the Sleipner field before and after CO_2 injection (baseline and monitor), and the corresponding rock physics models, we perform an extended sensitivity study. We show that prior information is crucial, especially in the monitor case. We demonstrate that joint inversion of seismic and CSEM data is also key to quantify CO_2 saturations properly. We finally apply the full inversion strategy to real data from Sleipner. We obtain rock frame moduli, porosity, saturation and patchiness exponent distributions and associated uncertainties along a 1D profile before and after injection. The results are consistent with geology knowledge and reservoir simulations, i.e., that the CO_2 saturations

are larger under the caprock confirming the CO_2 upward migration by buoyancy effect. The estimates of patchiness exponent have a larger uncertainty, suggesting semi-patchy mixing behaviour.

INTRODUCTION

For large-scale CO_2 storage projects, international regulations require the operator to set up a suitable Measurement, Monitoring and Verification (MMV) plan both during and after CO_2 injection (Pawar et al., 2015). The objectives of such a plan are to ensure conformance, containment, and early implementation of mitigation measures in case of leakage (Dean and Tucker, 2017). Conformance verification requires demonstrating a good understanding of the CO_2 behavior in the storage complex. This can be achieved by comparing model-based forecasts to monitoring measurements describing the CO_2 plume. In practice, geophysical measurements often play a key role in conformance verification. In this context, seismic and/or CSEM (controlled source electromagnetic) surveys combined with proper imaging methods offer the possibility to derive CO_2 saturation or other relevant rock physics properties (Ghosh et al., 2015; Dupuy et al., 2017).

Joint inversion of CSEM and seismic data can be approached using structural or/and petrophysical constraints. To favor structural similarity, Gallardo and Meju (2007) suggest adding a cross-gradient term to the misfit function otherwise only consisting of the sum of data misfits for the independent methods. Joint inversion with structural constraints has been applied for salt imaging, where seismic migration is challenging due to high attenuation in salt bodies and where CSEM can help mitigate such imaging challenges (Colombo et al., 2014; Ceci et al., 2014; Colombo et al., 2018). For the petrophysically constrained joint inversion, the coupling focuses on estimating rock physics properties using known cross-relationships between these reservoir parameters and seismic and CSEM data (Hoversten et al., 2006; Du and MacGregor, 2010). Combining both structural and petrophysical coupling is investigated by Abubakar et al. (2012) and Colombo and Rovetta (2018) while

constraining seismic imaging by rock physics relationships is also explored in recent papers (Aragao and Sava, 2020). Giraud et al. (2019) propose to account for uncertainties in joint inversion through a Bayesian framework. More generally, Dell'Aversana (2014) provides an extensive review of geophysical joint inversion approaches. For CO_2 storage monitoring, existing literature is limited to joint inversion of electrical resistivty tomography (ERT) and seismic data with structural coupling at Ketzin and at CaMI FRS (Containment and Monitoring Institute Field Research Station) (Jordan et al., 2018; Rippe et al., 2018), constrained CSEM inversion with seismic inversion results at Sleipner (Eliasson et al., 2014) and joint rock physics inversion on CSEM and seismic data at Sleipner (Subagjo et al., 2018).

The quantitative workflow described here is a joint rock physics inversion approach and uses a combination of geophysical and rock physics inversion methodologies (Dupuy et al., 2016c). Geophysical inversion typically provides estimates of macroscale properties such as seismic velocities, density or resistivity, while the rock physics inversion allows deriving meso- to micro-scale properties such as rock frame and fluid parameters (Dupuy et al., 2016a). However, the inverse problems associated with the first (geophysical inversion) and second (rock physics inversion) steps are non-linear, highly under-determined and ill-posed. Uncertainty evaluation is therefore of critical importance for proper monitoring and decision-making associated with conformance verification. A CO_2 storage site operator might take critical decisions such as stopping injection or adapting the injection strategy based on the monitoring results.

One way to allow for uncertainty evaluation consists in using a Bayesian formulation for both inversion steps (Tarantola, 2005). The geophysical inversion step based on, e.g., methods like Full Waveform Inversion (FWI) or CSEM inversion, is often carried out using gradient-based local optimization techniques. The uncertainty estimation can in this

case be performed using ensemble methods (Thurin et al., 2019) or with the computation and analysis of the inverse of the Hessian (or the second derivative of the distance to be minimized with respect to the model parameters). It can be interpreted as the posterior covariance matrix in a local probabilistic sense (Eliasson and Romdhane, 2017). This approach generates of a set of equivalent models, all explaining similarly well observed data and prior knowledge. The inversion results (quantities plus associated uncertainties) derived from this first step are typically seismic velocities or impedances, density, and resistivity. Those results can be used as input for the second inversion step, the rock physics inversion, which will be the focus of this paper.

Numerous approaches have been developed and applied in the last decades to carry out rock physics inversion for seismic reservoir characterization. Seismic reservoir characterization is the generation of reservoir structure and properties using seismic data. We do not intend to give a full review of the available rock physics inversion approaches. The readers are referred to Doyen (2007) and Bosch et al. (2010) for an exhaustive overview including geostatistical methods to estimate rock physics properties. In addition, Avseth et al. (2005) provide a good introduction to quantitative interpretation methods, while Mavko et al. (2009) and Guéguen and Palciauskas (1994) are useful books to understand the theoretical background and applicability of the wide range of available rock physics models.

To estimate rock physics properties from seismic data or inversion results, one has to solve an inverse problem where a distance (or a misfit function) is minimized. Because the forward problems are usually analytic and very quick to compute, global optimization or semi-global optimization techniques can be used. A full range of algorithms, including simulated annealing, genetic algorithms, and the neighbourhood algorithm, have been developed from the initial Monte-Carlo approach. Coléou et al. (2005) use seismic AVO

(amplitude versus offset) attributes to derive porosity estimates in a rock physics inversion framework. Grana et al. (2012) also formulate the optimization problem in a stochastic manner while Dupuy et al. (2016c) and Dupuy et al. (2016b) use the neighbourhood algorithm (Sambridge, 1999a) to determine the distribution of rock physics parameters without linearizing the forward operator. When compared to local optimization techniques, direct search (i.e, derivative free) optimization schemes offer the possibility to avoid convergence towards local minima when the misfit function has a complex shape. However, obtaining statistically meaningful information requires a careful sampling including both "good" and "bad" data-fitting models.

Probabilistic sampling, or importance sampling, can provide multiple realizations of prior and posterior distributions (Tarantola, 2005). Mosegaard and Tarantola (1995) explain that obtaining a maximum likelihood model is not sufficient to quantify uncertainty. For a model space with a large number of dimensions, it is necessary to generate a collection of equivalent models from the posterior distribution using a sampling algorithm (Metropolis algorithm in this case). The pioneering work of Sambridge and Mosegaard (2002) give a first review of sampling algorithms for geoscience applications. Oh and Kwon (2001) propose an implementation of Markov Chain Monte Carlo (MCMC) to infer information from posterior distributions of resistivity data derived by simulated annealing. Gunning and Glinsky (2007) compute the posterior distribution using MCMC but parametrize the model space with additional parameters to analyze reservoir quality. More recently, de Figueiredo et al. (2017) propose a Bayesian inversion combining linearized seismic AVO and rock physics inversion considering multi-modal prior distributions. In case of prior information in the form of Gaussian mixtures, they show that the use of a Gibbs sampler is required for sampling the posterior distribution and analyzing the uncertainty. Fjeldstad and Grana

(2018) also consider Gaussian mixtures for prior models to invert for rock-fluid classes. Jullum and Kolbjørnsen (2016) use a similar approach to derive rock physics properties from reflection data via a MCMC sampling algorithm using Sleipner poststack data after simplifying and linearizing the rock physics model.

Instead of linearizing the forward model, our approach uses a complete rock physics model and applies the two-stage workflow proposed by Sambridge (1999a,b), combining search and importance sampling stages to estimate selected rock physics parameters with uncertainty assessment. We first recall the Bayesian inversion method before describing the neighbourhood algorithm used for the search and appraisal stages of the second inversion step (rock physics inversion). We then present the CO_2 storage monitoring context and the associated rock physics models. In the third section, we show sensitivity tests and discuss the importance of prior information. We then demonstrate the workflow on a real data example from the Sleipner field where we combine inputs from seismic and CSEM inversions to derive rock frame properties, fluid saturations and distributions. Finally, we discuss limitations and possible improvements of the proposed approach.

THEORY

Bayesian inversion method

Our proposed two-step approach combines independent inversion of geophysical data with rock physics inversion. The use of a Bayesian formulation is motivated by the need to incorporate prior information and uncertainties in both steps. Bayesian inference consists in using Bayes' theorem to update a prior probability distribution to a posterior one by making use of new (observed) information (Tarantola, 2005). The solution to a Bayesian

inverse problem can be written as:

$$\rho_{post}(\boldsymbol{m}) \propto \rho_{prior}(\boldsymbol{m})\ L\left(\boldsymbol{m}|\boldsymbol{d_{obs}}\right), \tag{1}$$

where $\boldsymbol{m}$ is the model parameter vector to be estimated, $\rho_{post}(\boldsymbol{m})$ is the posterior probability density function (PDF), and $\rho_{prior}(\boldsymbol{m})$ is the prior PDF describing our initial knowledge about the model parameters. $L\left(\boldsymbol{m}|\boldsymbol{d_{obs}}\right)$ denotes the data likelihood function describing the probability of having a model $\boldsymbol{m}$, given observation $\boldsymbol{d_{obs}}$. This probability depends on the fit between the observations and predictions for a given model $\boldsymbol{m}$.

For simplicity, we assume that the prior PDF can be described by a multidimensional Gaussian distribution, but our approach for the rock physics inversion step is not limited to this assumption. We define $\rho_{prior}(\boldsymbol{m})$ as

$$\rho_{prior}(\boldsymbol{m}) \propto \exp\left(-\frac{1}{2}\ \left(\boldsymbol{m}-\boldsymbol{m_0}\right)^T\ \boldsymbol{C_{m_{prior}}}^{-1}\ \left(\boldsymbol{m}-\boldsymbol{m_0}\right)\right), \tag{2}$$

where $\boldsymbol{m_0}$ and $\boldsymbol{C_{m_{prior}}}$ denote the prior mean model and the prior model covariance, respectively. The data likelihood function can be described by first defining the misfit $\zeta(\boldsymbol{m})$ between observed and modeled data such as

$$\zeta(\boldsymbol{m}) = \left(\boldsymbol{d_{obs}} - g(\boldsymbol{m})\right)^T\ \boldsymbol{C_d^{-1}}\ \left(\boldsymbol{d_{obs}} - g(\boldsymbol{m})\right). \tag{3}$$

Here, $\boldsymbol{C_d}$ is the data covariance matrix describing uncertainties and correlations in observed data. The operator ^{T} is the transpose (or conjugate transpose in case of complex entries) and $g(\boldsymbol{m})$ denotes a general (linear or non-linear) forward modeling operator describing the

link between a (predicted) data vector $\boldsymbol{d}$ and a model vector $\boldsymbol{m}$:

$$\boldsymbol{d} = g(\boldsymbol{m}). \tag{4}$$

Assuming that the data likelihood function also follows a multidimensional Gaussian distribution, we can write:

$$L\left(\boldsymbol{m}|\boldsymbol{d_{obs}}\right) \propto \exp\left(-\frac{1}{2}\,\zeta(\boldsymbol{m})\right). \tag{5}$$

In the geophysical domain, $g(\boldsymbol{m})$ is the operator linking geophysical data (e.g., pre-stack seismic data or electromagnetic data) to selected geophysical properties (e.g., seismic velocities or resistivities) for a given acquisition. For FWI and CSEM methods, it corresponds to the numerical solutions of the acoustic wave equation and the Maxwell equations at the receiver locations, respectively. Solving the associated inverse problem requires dealing with a large-scale non-linear inverse problem where only local or ensemble-based optimization techniques are tractable in terms of computational requirements (Virieux and Operto, 2009). One efficient way of approximating the posterior PDF consists in linearizing the forward modeling operator around the maximum *a posteriori* model $\boldsymbol{m_{LSI}}$ that can be derived with least square inversion techniques (Tarantola, 2005). The posterior can then be approximated with a multidimensional Gaussian distribution such as

$$\rho_{post}(\boldsymbol{m}) \propto \exp\left(-\frac{1}{2}\left(\boldsymbol{m}-\boldsymbol{m_{LSI}}\right)^T\ \boldsymbol{C_{m_{post}}}^{-1}\ \left(\boldsymbol{m}-\boldsymbol{m_{LSI}}\right)\right), \tag{6}$$

where the posterior model covariance $\boldsymbol{C_{m_{post}}}$ can be calculated as a reduction of the prior model covariance using the information gained from the geophysical inversion (Duffet and

Sinoquet, 2006; Zhu et al., 2016; Eliasson and Romdhane, 2017). Posterior covariance analysis is useful for assessing uncertainty in the velocity or resistivity models obtained by FWI or CSEM inversion. The posterior (model) covariance matrix $\boldsymbol{C_{m_{post}}}$ obtained after the first inversion step (FWI and CSEM) is used as the prior (data) covariance matrix in the second inversion step (rock physics inversion). This is a convenient way to propagate uncertainty in both steps. For more details on the workflow, see Dupuy et al. (2021).

In the rock physics domain, $g(\boldsymbol{m})$ is the operator linking geophysical properties to rock physics properties $\boldsymbol{m}$ (e.g., porosity, pore pressure and fluid saturation) and is usually referred to as the rock physics model. Similarly to the first step, a data fitting process is carried out between modeled rock physics properties and observed data, corresponding to geophysical properties. We use the Gassmann (1951) rock physics model with an effective fluid phase calculated according to the Brie et al. (1995) equation. Similar to the first step, the function $g(\boldsymbol{m})^{-1}$ cannot be explicitly derived in the case of multiphase pore fluids. However, given the low computational requirement of the forward model, the inverse problem can be solved with global or semi-global optimization algorithms such as Monte-Carlo or the neighbourhood algorithm (NA) (Sambridge, 1999a). In our approach, we use the NA following the work of Dupuy et al. (2017) and we describe the misfit between observed and modeled data using equation 3, where $\boldsymbol{C_d}$ is the data covariance matrix describing data noise statistics and equal to the posterior covariance matrix derived after FWI or CSEM inversion. In the examples discussed below, the model parameters $\boldsymbol{m}$ are selected rock physics properties, the rock physics model function is denoted by g, while observed data $\boldsymbol{d_{obs}}$ are geophysical properties from the geophysical inversion step (using for example FWI and/or CSEM). The data covariance is therefore described by the posterior covariance matrix from the first (geophysical inversion) step.

Neighbourhood Algorithm: search and importance sampling

In this work, both search and appraisal stages described in Sambridge (1999a) and Sambridge (1999b) are used. The first stage is a direct (i.e., derivative free) guided search exploring the model space and calculating the misfit between modeled $g(\boldsymbol{m})$ and observed $\boldsymbol{d_{obs}}$ data following equation 3. It is aimed at efficiently finding an ensemble of models that sample the "good" data fitting regions of the parameter space using the geometric properties of the Voronoï cells. The Voronoï diagram allows to divide a multi-dimensional model space into convex polyhedra (cells) which are the nearest neighbour regions of the samples calculated with a given distance measure (L2 norm in NA). In Bayesian inference, we do not only look for the most likely model, but for the probability of all models. Consequently, a thorough exploration of the whole model space is necessary. The NA has excellent properties in terms of exploration of large parts of the model space combined with convergence towards high likelihood models.

The main advantage of the NA search stage is the way that the search algorithm is parametrized, i.e., with only three parameters allowing exploration of the model space in a smart and efficient way. The search stage is parametrized by the number of iterations n_{iter}, the number of samples generated at each iteration n_{samp} and the number of resampled cells at each iteration n_{cell}. At the first iteration, n_{samp} models are selected in the model space following a uniform distribution between minimum and maximum values for each inverted parameter. At each iteration, probability density (misfit) is calculated for each sample (model) considering data likelihood and prior distributions (equations 1 and 3). Among these n_{samp} models, n_{cell} samples with the highest PDF (lowest misfit) are selected. Around these n_{cell} samples, n_{samp} new models equally distributed in the Voronoï cells are

generated. These cells are built from the samples of the previous iterations and depend on the neighbouring cells via the Voronoï diagram. At the end, n_{iter} x n_{samp} models are generated with a good sampling concentration in the promising regions of the model space. The convergence properties will depend on the choice of the exploration parameters (n_{iter}, n_{samp} and n_{cell}). For example, if n_{cell} is low and n_{iter} is high, the search will be more local and more models will be found close to the global minimum, while if n_{cell} is high and n_{iter} is low, the search will be wider and explore more the model space. The best compromise between the three parameters is application dependent and is intensively tested for rock physics inversion (Dupuy et al., 2016c).

The second stage can be referred to as the appraisal/importance sampling stage. It answers the need to infer statistically meaningful information (e.g., trade-offs, resolution and confidence intervals) from the ensemble of models generated during the search stage. The approach proposed in Sambridge (1999b) relies on a Bayesian point of view. During the importance sampling, no additional forward problems are solved. The Voronoï cells are also used at this stage but to construct a multi-dimensional interpolant of the misfit measure and efficiently approximate the posterior PDF $\rho_{post}(\boldsymbol{m})$ (representing the information contained in the ensemble of models):

$$\rho_{NA}(\boldsymbol{m}) \approx \rho_{post}(\boldsymbol{m}) \ . \tag{7}$$

The neighborhood approximation of the PDF $\rho_{NA}(\boldsymbol{m})$ can then be used for the evaluation of Bayesian integrals and derive relevant statistical indicators such as posterior mean model, posterior model covariance matrix, resolution matrix and marginal distributions. Prior model probability distributions can be easily integrated in the post-Bayesian analysis step.

The appraisal stage requires the generation of a (new) resampled ensemble distributed

according to the approximate PDF $\rho_{NA}(\boldsymbol{m})$. Sambridge (1999b) suggests the use of a Gibbs sampler and discuss in detail the main factors influencing the computational burden of the appraisal stage. The tuning parameters for this stage are the number of random walks n_{walks} and the number of steps n_{steps} for each random walk. They are often derived by trial and error. After each trial, the convergence of the sampler can be checked by computing the potential scale reduction factor (PSR factor, (Gelman et al., 2013)). The dependency of the results on the starting points used for each random walk can also be analysed to verify the reliability of the estimated distributions.

CO_2 STORAGE MONITORING: CONTEXT AND MODELS

Sleipner case study

Sleipner is the oldest CO_2 storage site in activity. In the North Sea, offshore Norway, approximately one million tonnes of CO_2 per year have been injected into the Utsira saline aquifer since 1996. Regular seismic surveys have been acquired since 1994, before the start of the injection. In this study, we used baseline (1994) and monitor (2008) vintages for a real data case study. The Utsira sandstone has very good reservoir quality thanks to its high permeability and high porosity. It is also an extensively studied rock formation, allowing several of the rock physics parameters to be determined with good confidence.

The mineralogical composition is a mix of seven minerals, with mainly quartz (75%), K-feldspar (13%), and other minerals (calcite, albite, aragonite and mica) in smaller proportions (3% each) (Chadwick et al., 2004). Effective grain density is calculated by mass weighted average while the effective grain bulk modulus is calculated by averaging Hashin and Shtrikman (1963) bounds based on the mineral composition of the Utsira sandstone.

Pore fluid properties (brine for the baseline case and brine mixed with supercritical CO_2 for the monitor case) depend on pore pressure, temperature and salinity, which are well-known at Sleipner (Ghaderi and Landrø, 2009). We use the Utsira reservoir pressure and temperature ($37°C$ and $11MPa$) to calculate brine and CO_2 properties with empirical equations (Batzle and Wang, 1992) and with equations of state (Span and Wagner, 1996; Lindeberg, 2013). We use the available information to define prior distributions of the grains (K_S and ρ_S) and fluid (K_w, ρ_w, K_{CO_2} and ρ_{CO_2}) properties described in the following subsection.

Rock physics models

In this section, we describe the forward modeling operator g which is a set of analytical non-linear relations linking rock physics parameters, describing the properties of interest, and geophysical data (seismic, gravimetry, CSEM and/or electrical data). Extensive literature is available to build relevant rock physics models. The approaches range from simple to quite complex and can be empirical or more generic. For CO_2 storage in high porosity sandstone aquifers, generic Gassmann (1951)'s relations for seismic data and Archie (1942)'s law for electrical properties are adopted in many papers (Dupuy et al., 2017; Falcon-Suarez et al., 2018). The seismic velocities (P-wave velocity V_P and S-wave velocity V_S) can be described with respect to bulk and shear moduli (here undrained bulk modulus K_U and undrained shear modulus G_U) as:

$$V_P = \sqrt{\frac{K_U + 4G_U/3}{\rho}}, \tag{8}$$

$$V_S = \sqrt{\frac{G_U}{\rho}}. \tag{9}$$

The bulk density ρ is usually calculated as a weighted average over the fluid and solid components of the porous medium:

$$\rho = (1-\phi)\ \rho_S + \phi\ \rho_f, \tag{10}$$

where ϕ is the porosity, ρ_S and ρ_f are the grains and fluid density, respectively. The mechanical moduli K_U and G_U are derived from the Gassmann (1951)'s equations:

$$K_U = \frac{\phi\ K_D + (1-(1+\phi)\ K_D/K_S)\ K_f}{\phi\ (1+\Delta)}, \tag{11}$$

$$G_U = G_D, \tag{12}$$

with the additional parameter Δ is defined as:

$$\Delta = \frac{1-\phi}{\phi}\frac{K_f}{K_S}\left(1-\frac{K_D}{(1-\phi)\ K_S}\right). \tag{13}$$

Together with the porosity ϕ, the dry bulk modulus K_D and the dry shear modulus G_D describe the rock frame (drained state). The bulk modulus K_f of the fluid saturating the pores and the bulk modulus K_S of the grains are the additional parameters used in Gassmann's equations for a saturated porous medium (with one fluid phase). Equations 8 to 13 are sufficient to establish an adequate link between the most relevant rock physics and elastic properties for a baseline case (before CO_2 injection). Table 1 summarizes these properties and related input data.

With the injection of CO_2, the pores of the Utsira sandstone will be partially filled with brine and supercritical CO_2 (given the reservoir pressure and temperature conditions at Sleipner). The most common way to account for partial saturation is to derive properties

of an effective fluid phase that can be plugged into Gassmann's equations (normally defined for a single fluid in the pores). The effective fluid density ρ_f is calculated with respect to brine ρ_w and CO_2 ρ_{CO_2} densities and CO_2 saturation S_{CO_2} as:

$$\rho_f = (1 - S_{CO_2})\ \rho_w + S_{CO_2}\ \rho_{CO_2}. \tag{14}$$

The effective fluid bulk modulus K_f is a critical parameter and can be calculated in different ways. Dupuy et al. (2017) show that using the Brie et al. (1995) equation is a convenient way to span the different models by introducing an additional degree of freedom via the exponent e. This exponent is called Brie exponent or patchiness exponent as it corresponds to uniform mixing of fluid phases for large values (up to 40) and patchy mixing for values tending towards 1. The Brie equation is then expressed with respect to brine bulk modulus K_w and CO_2 bulk modulus K_{CO_2} as well as patchiness exponent e and CO_2 saturation S_{CO_2}:

$$K_f = (K_w - K_{CO_2})\ (1 - S_{CO_2})^e + K_{CO_2}. \tag{15}$$

In addition to the 2008 seismic data, we consider also CSEM data (acquired in the same year) to derive bulk resistivity R_t. The common way to link resistivity with rock physics parameters is to use the Archie (1942)'s law. This formula expresses the resistivity with respect to porosity ϕ, CO_2 saturation S_{CO_2}, brine conductivity σ_w, cementation exponent m and saturation exponent n as:

$$R_t = \frac{\phi^{-m}(1 - S_{CO_2})^{-n}}{\sigma_w}. \tag{16}$$

The parametrization and the associated geophysical observables for the monitor case (partial saturation due to the CO_2 injection) are summarized in Table 1. Part of these rock physics properties can be estimated a priori from geological knowledge, log data or baseline inversions (Yan et al., 2019) as shown in the real data application section.

SYNTHETIC SENSITIVITY TESTS

Search and appraisal stages

Figures 1 and 2 present examples of derived rock physics inversion results after search and appraisal stages. For both cases, the input data is a vector with two entries corresponding to bulk density and P-wave velocity values. The output vector is a 7x1 vector with the rock physics properties described in Table 1. This test corresponds to the sensitivity test for the baseline data shown in the following section. For this test, we consider a total number of samples corresponding to $n_{samp} = 300$ resampled models for $n_{iter} = 100$ iterations, i.e., 30 300 models (knowing that 300 models are drawn randomly in the model space at the first iteration) for the search stage. For the appraisal stage, the convergence is reached after a total of $n_{models} = 800,000$ resampled models corresponding to $n_{walks} = 10,000$ random walks and a maximum of $n_{steps} = 80$ steps for each walk.

Selected 2D sections of the model space are displayed after the search (top panels) and appraisal stages (bottom panels) in Figures 1 and 2. For the results of Figure 1, a bounded uniform distribution of the inverted properties is assumed (i.e., very weak prior information). Figure 2 shows the same results when the prior information about the inverted parameters is described by normal distributions with properties given in Table 2. The prior PDF is multiplied by the data likelihood following equation 1. The results of the appraisal stages

Table 1: Parameters (model space) and input data for the baseline and monitor cases. In the baseline case, the porous medium is fully brine saturated so the model space is limited to seven parameters: K_S, ρ_S, K_f, ρ_f, ϕ, K_D and G_D. The input data is also limited to seismic data for the baseline case, i.e., only V_P and ρ.

Estimated parameters			
Grains parameters			
Name	Bulk modulus	Density	
Symbol	K_S	ρ_S	
Unit	GPa	kg/m^3	
Brine parameters			
Name	Bulk modulus	Density	
Symbol	K_w	ρ_w	
Unit	GPa	kg/m^3	
CO_2 parameters			
Name	Bulk modulus	Density	
Symbol	K_{CO_2}	ρ_{CO_2}	
Unit	GPa	kg/m^3	
Dry rock frame parameters			
Name	Porosity	Bulk modulus	Shear modulus
Symbol	ϕ	K_D	G_D
Unit		GPa	GPa
Archie parameters			
Name	Brine conductivity	Cementation exponent	Saturation exponent
Symbol	σ_w	m	n
Unit	S/m		
Partial saturation parameters			
Name	CO_2 saturation	Patchiness exponent	
Symbol	S_{CO_2}	e	
Unit			
Input data			
Seismic data			
Name	P-wave velocity	Bulk density	
Symbol	V_P	ρ	
Unit	m/s	kg/m^3	
EM/electrical data			
Name	Bulk resistivity		
Symbol	R_t		
Unit	$\Omega.m$		

(bottom parts of the figures) show the distribution of resampled models assuming equal likelihood. This resampled distribution allows to calculate Bayesian integrals and derive marginal probabilities, resolution matrices and confidence intervals. It is worth noting that, similar to Sambridge (1999b) observations, the spread of the models is wider after appraisal stage than after the search stage. Consequently, the ensemble of models obtained after the search stage and the derived marginal PDF may give a false impression of accuracy.

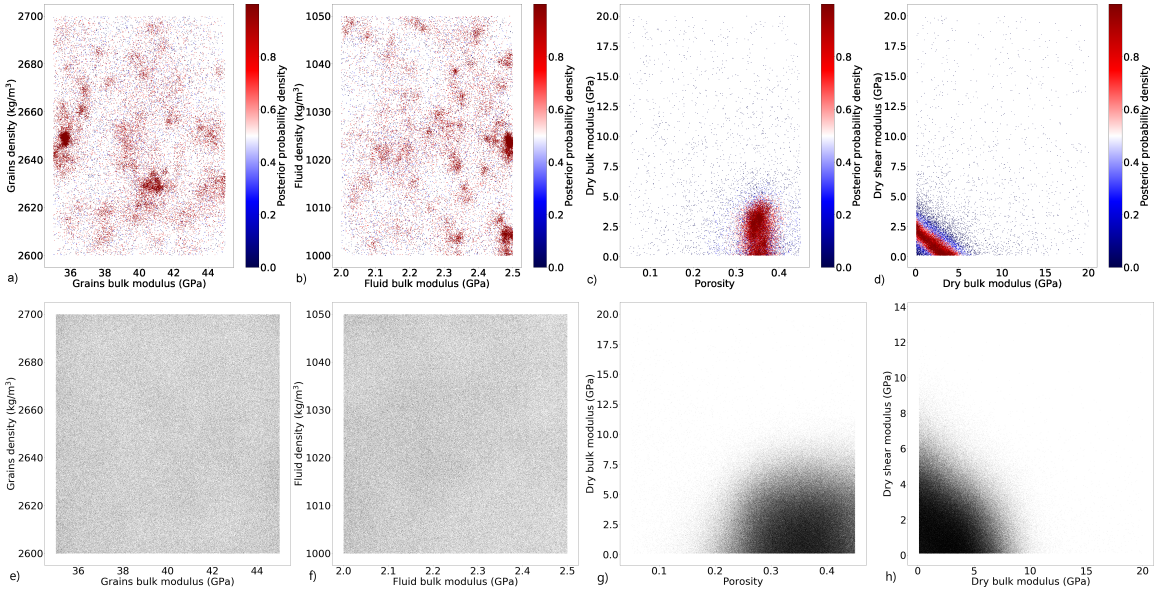

Figure 1: Bayesian rock physics inversion results after search and appraisal stages. The top line gives the distribution of models with associated PDF after the search stage (a-d). The bottom line gives all resampled models after the appraisal stage (all models are equally likely after sampling) (e-h). The results are given for a case where seven rock physics parameters are inverted: (a,e) grains density and grains bulk density, (b,f) fluid density and fluid bulk modulus, (c,g) dry bulk modulus and porosity and (d,h) dry shear modulus and dry bulk modulus. The input data are P-wave velocity V_P and bulk density ρ. Prior information assumes a bounded uniform distribution for each parameter. The inversion ranges are given in Table 2.

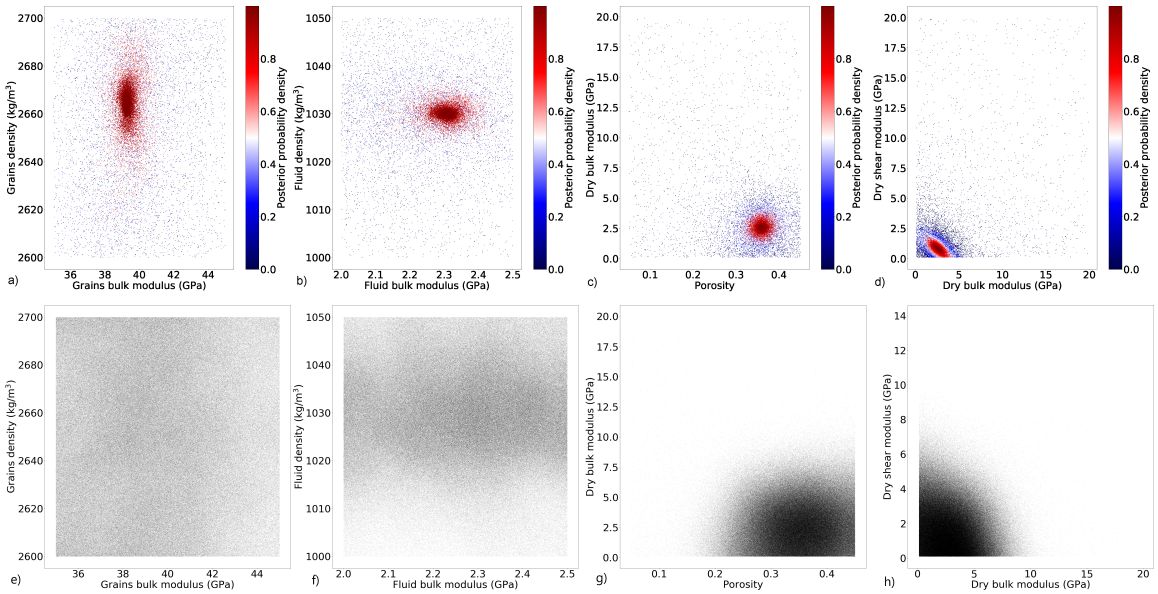

Figure 2: Bayesian rock physics inversion results after search and appraisal stages. The top line gives the distribution of models with associated PDF after the search stage (a-d). The bottom line gives all resampled models after the appraisal stage (all models are equally likely after sampling) (e-h). The results are given for a case where seven rock physics parameters are inverted: (a,e) grains density and grains bulk density, (b,f) fluid density and fluid bulk modulus, (c,g) dry bulk modulus and porosity and (d,h) dry shear modulus and dry bulk modulus. The input data are P-wave velocity V_P and bulk density ρ. The prior distributions are applied to the PDF calculated during the search stage and are based on normal distributions with properties given in Table 2 along with the inversion ranges.

Parametrization and prior models

We run a set of realistic synthetic tests to infer the best parametrization and input data choice for the Sleipner real data (following section). We test both baseline and monitor cases using the rock physics models defined in the previous section. For the monitor tests, we compare the derived results for different cases involving: (1) uniform and normal prior distributions, (2) parameters fixed to their true value (to reduce the size of the model space); (3) low and high CO_2 saturation, and (4) different input data (seismic only or seismic and CSEM).

For the baseline case, the seven rock physics parameters are inverted from P-wave velocity and bulk density input data, considering the cases of truncated (between minimum and maximum values) uniform (Figure 3) and Gaussian prior distributions (mostly on grains and fluid properties, Figure 4). The prior distributions are also displayed for comparison. Table 2 gives the parameter ranges and the prior properties.

The posterior PDF (visualized using 1D and 2D marginal distributions) is improved (uncertainties reduced) when stronger prior information is included (Gaussian prior). The uncertainty of rock frame properties (dry bulk and shear moduli and porosity) is reduced mainly thanks to better constraints (stronger prior information) on the four other parameters (grains and fluid properties). These four parameters have stronger prior information but the uncertainty on their inverted values is large (Figure 4), mainly because the seismic input data (P-wave velocity and density) are weakly sensitive to these parameters (Dupuy et al., 2016c).

In a second stage, the results from the inversion of the baseline data are used to define prior distributions for the monitor case, by assuming truncated Gaussian distributions centered around true values with properties given in Table 3. In these sensitivity tests, we assume that the baseline results help to decrease the standard deviation and that we have less uncertainty on the fluid, grains and rock frame parameters. For the following real data case, the posterior PDF from the baseline inversion is used as prior PDF and 99% confidence intervals are selected from the baseline PDF to define model space limits for the monitor case.

Figures 5 and 6 show the Bayesian rock physics inversion results for the monitor case involving inversion for eleven rock physics parameters, assuming uniform and Gaussian

prior distributions, respectively. We select prior distribution following truncated Gaussian distributions with mean centered around true value and a standard deviation more or less large depending on the knowledge we expect to have on each parameter. For example, the grain properties of the Utsira sands are well-known so we set up a small standard deviation. CO_2 saturation is the main driver of P-wave velocity changes and we set up a large standard deviation as we do not have a priori information on this parameter.

Significant changes of 1D marginal probabilities for S_{CO_2} saturation and for the patchiness exponent e can be observed, with a better convergence towards true values of CO_2 saturation and patchiness exponent ($S_{CO_2} = 0.2$ and $e = 5$) when Gaussian prior is included (Figure 6). The 1D marginal distribution for the rock frame properties and the porosity are also slightly improved in Figure 6 compared to Figure 5, suggesting rather low moduli and high porosity (approximately 35%) with low uncertainty. Significant changes for most of the 2D marginal probabilities can be noted with a clear Gaussian shape when normal distributions are considered for the prior information. These relative large uncertainties (large standard deviation) for the parameters can be interpreted from the ambiguity in saturation-patchiness exponent relation to P-wave velocity (see next section).

Figure 7 displays the inversion results when the prior information is described with normal distributions as given in Table 3 for K_D, G_D, ϕ, S_{CO_2} and e. Compared to the case of Figure 6, the other parameters (K_S, ρ_S, K_w, ρ_w, K_{CO_2}, and ρ_{CO_2}) are fixed to their true values. The derived 1D marginal probabilities for S_{CO_2} and e are consistent with the true values ($S_{CO_2} = 0.2$ and $e = 5$) although the CO_2 saturation is slightly overestimated. Compared to Figure 6, the rock frame properties and porosity posterior PDF are also improved.

Figure 8 displays the results when the true CO_2 saturation is equal to $S_{CO_2} = 0.8$. Similar trends are obtained when compared to those of Figure 7. CO_2 saturation estimates (4^{th} column/row of Figure 8) are updated. One can note that the Gaussian shape of the S_{CO_2} marginal probability distribution is not as clean as the case with $S_{CO_2} = 0.2$ (Figure 7. This reflects the well-known trade-off between these the patchiness exponent and the CO_2 saturation which are difficult to discriminate when CO_2 saturation is high (Dupuy et al., 2017).

Figures 9 and 10 show the same tests when bulk resistivity R_t is used as an additional input (to P-wave velocity and density). In this case, the rock physics models include equation 16 (Archie's law), resulting in four additional inverted parameters. For simplicity, we assume the electrical properties (brine conductivity σ_w, cementation exponent m and saturation exponent n) to be known and fixed to their true values (Table 3).

The estimated marginal probability distributions, including S_{CO_2} and e, are significantly updated in Figure 10 when compared to the case shown in Figure 8. The peaks of the 1D marginals are consistent with true values and have a narrower spread. For $S_{CO_2} = 0.2$, the 1D marginal PDF shows an uni-modal normal-like shape with the peak around 0.2 and the 1D marginal probability distribution for e is also quite narrow (Figure 9). However, it is not a significant improvement compared to Figure 7 where only seismic data are used. Conversely, when CO_2 saturation is equal to 0.8 (Figure 10), the estimation of CO_2 saturation is strongly improved compared to Figure 8. The peak of the distribution is located close to the true value for the saturation and is more spread for the patchiness exponent. The resistivity is sensitive almost only to saturation (the other parameters in the Archie relation being fixed or have strong a priori) so it strongly constrains saturation, while the P-wave velocity drives the estimation of the patchiness exponent.

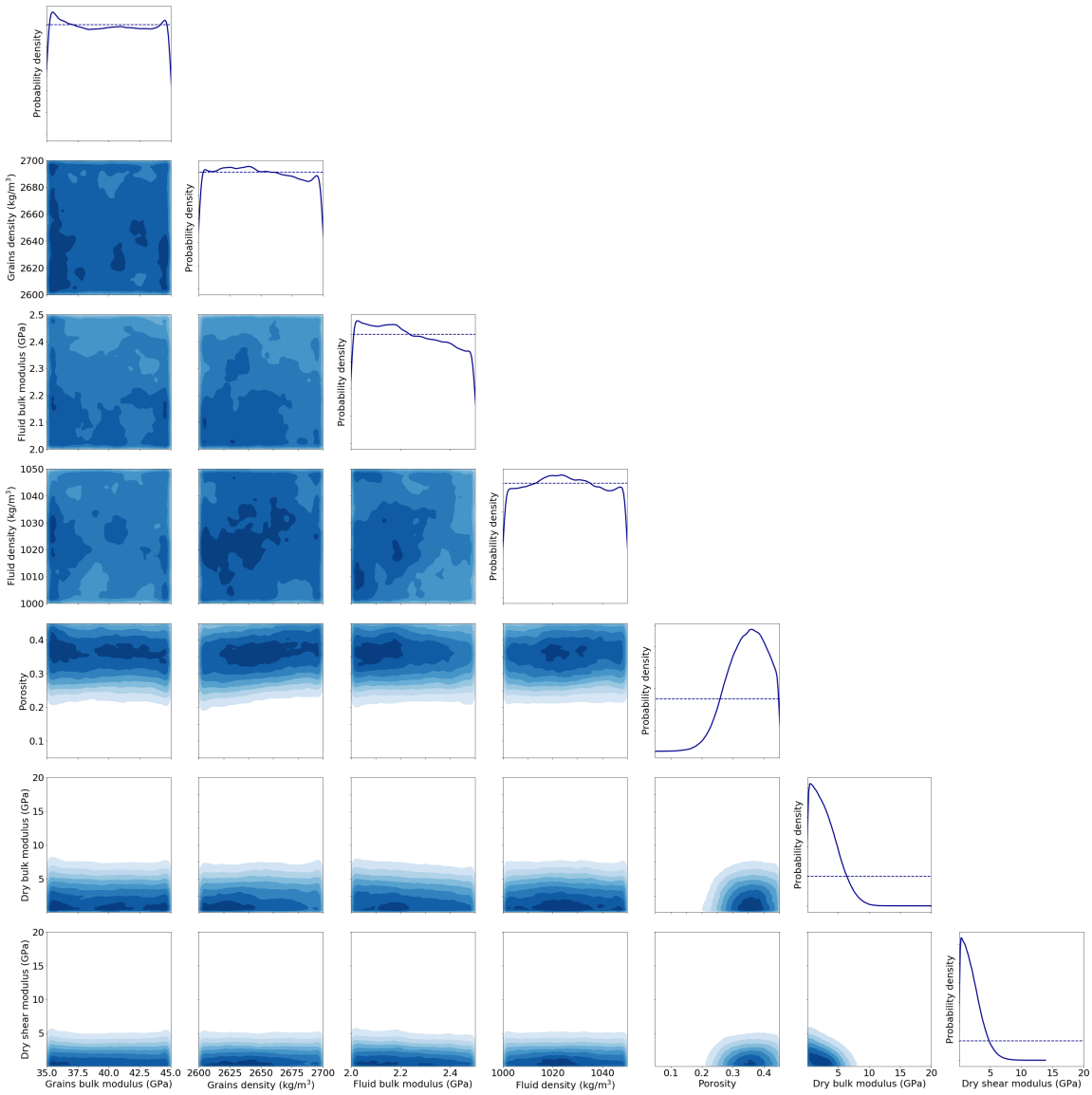

Figure 3: Baseline case - Uniform prior information - Input data = V_P, ρ.
Bayesian rock physics inversion results after search and appraisal stages. The prior information consists in uniform distributions between minimum and maximum values given in Table 2. The diagonal shows the 1D marginal posterior PDF in continuous blue lines and the 1D prior distribution in dashed blue lines, and the lower left half shows the 2D marginal posterior PDF. Posterior marginal distributions are calculated with kernel density estimates. The results are given for the baseline case where seven rock physics parameters are inverted. The input data are P-wave velocity V_P and bulk density ρ.

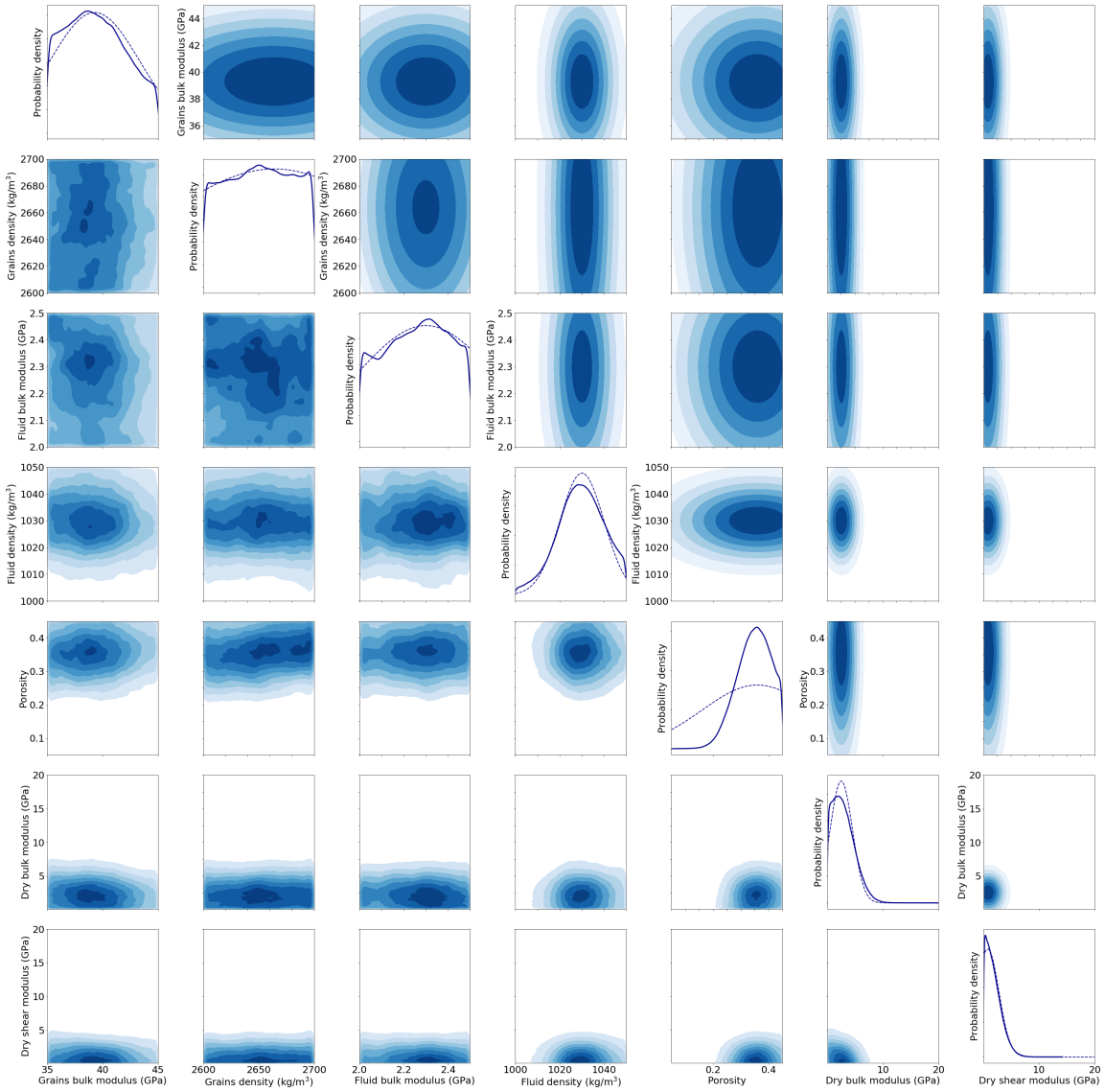

Figure 4: Baseline case - Gaussian prior information - Input data = V_P, ρ.
Bayesian rock physics inversion results after search and appraisal stages. The upper right half shows the 2D prior distributions (normal distributions with properties given in Table 2), while the diagonal shows the 1D marginal posterior PDF in continuous blue lines and the 1D prior distribution in dashed blue lines, and the lower left half shows the 2D marginal posterior PDFs. Posterior marginal distributions are calculated with kernel density estimates. The results are given for the baseline case where seven rock physics parameters are inverted. The input data are P-wave velocity V_P and bulk density ρ.

Table 2: Inversion ranges, prior properties for the normal distribution of baseline parameters and corresponding seismic data. Note that we have assumed strong prior information on grains (K_S and ρ_S) and fluid (K_f and ρ_f) parameters and little information on rock frame properties (ϕ, K_D and G_D). The inversion ranges are also the bounding values for prior distributions.

		$K_S(GPa)$	$\rho_S(kg/m^3)$	$K_f(GPa)$	$\rho_f(kg/m^3)$	ϕ	$K_D(GPa)$	$G_D(GPa)$
Inversion range	Min	35	2600	2	1000	0.05	0.1	0.1
	Max	45	2700	2.5	1050	0.45	20	20
Gaussian distribution	Mean (true value)	39.29	2664	2.3	1030	0.36	2.56	0.84
	Standard deviation	4	100	0.3	10	0.2	2	2
		$V_P(m/s)$	$\rho(kg/m^3)$					
Corresponding calculated data		2057	2076					

Table 3: Inversion ranges, prior properties for the normal distribution of monitor parameters and corresponding seismic and electrical data. Note that we have strong prior information on grains (K_S and ρ_S) and fluids (K_w, ρ_w, K_{CO_2} and ρ_{CO_2}) parameters and weaker information on rock frame properties (ϕ, K_D and G_D) from the baseline inversion. We have very little prior information on CO_2 saturation S_{CO_2} and patchiness exponent e. The inversion ranges are also the bounding values for prior distributions.

Seismic		$K_S(GPa)$	$\rho_S(kg/m^3)$	$K_w(GPa)$	$\rho_w(kg/m^3)$	$K_{CO_2}(GPa)$	$\rho_{CO_2}(kg/m^3)$
Inversion range	Min	39	2650	2.25	1025	0.07	680
	Max	40	2670	2.35	1035	0.08	715
Gaussian distribution	Mean (true value)	39.29	2664	2.3	1030	0.075	700
	Standard deviation	0.1	1	0.01	0.5	0.00005	0.5

Seismic		ϕ	$K_D(GPa)$	$G_D(GPa)$	S_{CO_2}	e
Inversion range	Min	0.05	0.1	0.1	0	1
	Max	0.45	20	20	1	40
Gaussian distribution	Mean (true value)	0.36	2.56	0.84	0.2 or 0.8	5
	Standard deviation	0.1	4	4	0.4	10

CSEM		ϕ	S_{CO_2}	$\sigma_w(S/m)$	m	n
Inversion range	Min	0.05	0	5.5	1	2
	Max	0.45	1	5.5	1	2
Gaussian distribution	Mean (true value)	0.36	0.8	5.5	1	2
	Standard deviation	0.1	0.4	0	0	0
Corresponding data		$V_P(m/s)$	$\rho(kg/m^3)$	$R_t(\Omega.m)$		
$S_{CO_2} = 0.2$		1648	2052	0.79		
$S_{CO_2} = 0.8$		1397	1981	12.63		

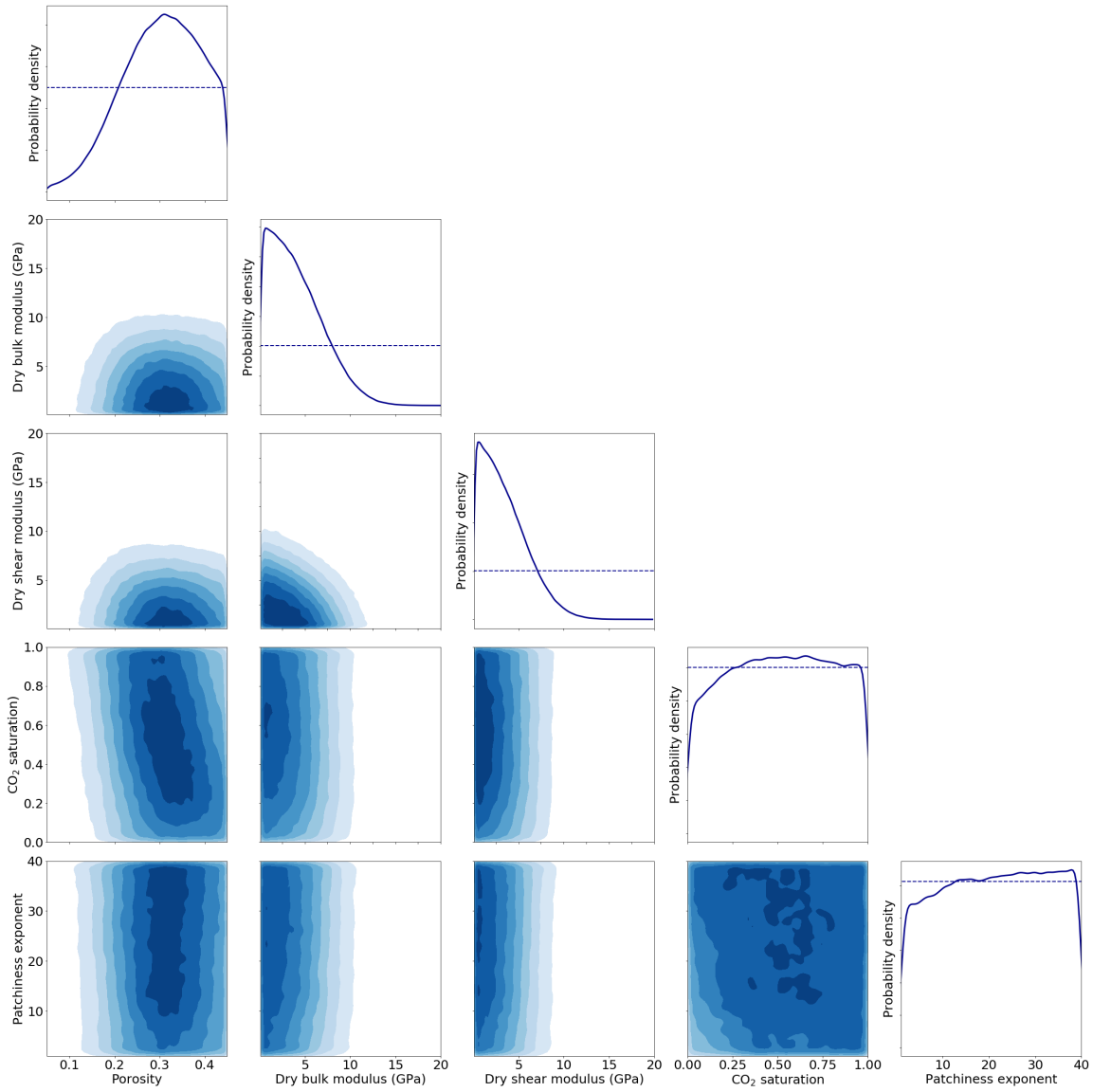

Figure 5: Monitor case - Uniform prior information - Input data = V_P, ρ.
Bayesian rock physics inversion results after search and appraisal stages. The prior information consists in uniform distributions between minimum and maximum values given in Table 3. The diagonal gives the 1D marginal distributions in continuous blue lines and the 1D prior distribution in dashed blue lines, and the lower left half gives the 2D marginal posterior PDFs. Posterior marginal distributions are calculated with kernel density estimates. The results are given for the monitor case where eleven rock physics parameters are inverted (the five most meaningful parameters are plotted). The input data are P-wave velocity V_P and bulk density ρ.

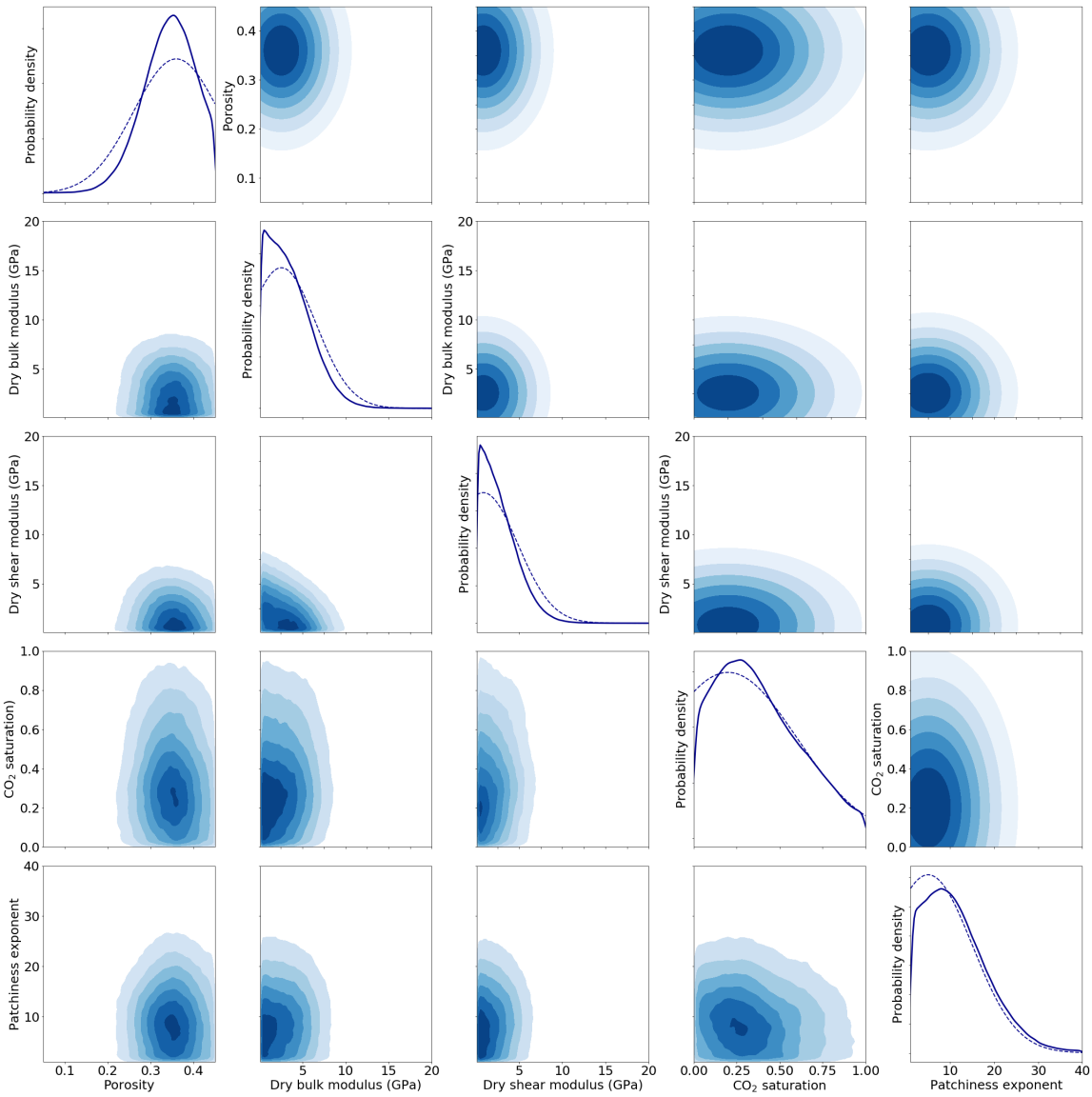

Figure 6: Monitor case - Gaussian prior information - Input data = V_P, ρ.
Bayesian rock physics inversion results after search and appraisal stages. The upper right half gives the 2D prior distributions (normal distributions with properties given in Table 3), while the diagonal gives the 1D posterior marginal distributions in continuous blue lines and the 1D prior distribution in dashed blue lines and the lower left half gives the 2D marginal posterior PDFs. Posterior marginal distributions are calculated with kernel density estimates. The results are given for the monitor case where eleven rock physics parameters are inverted (the five most meaningful parameters are plotted). The input data are P-wave velocity V_P and bulk density ρ. The prior distributions are normal distributions with properties given in Table 3.

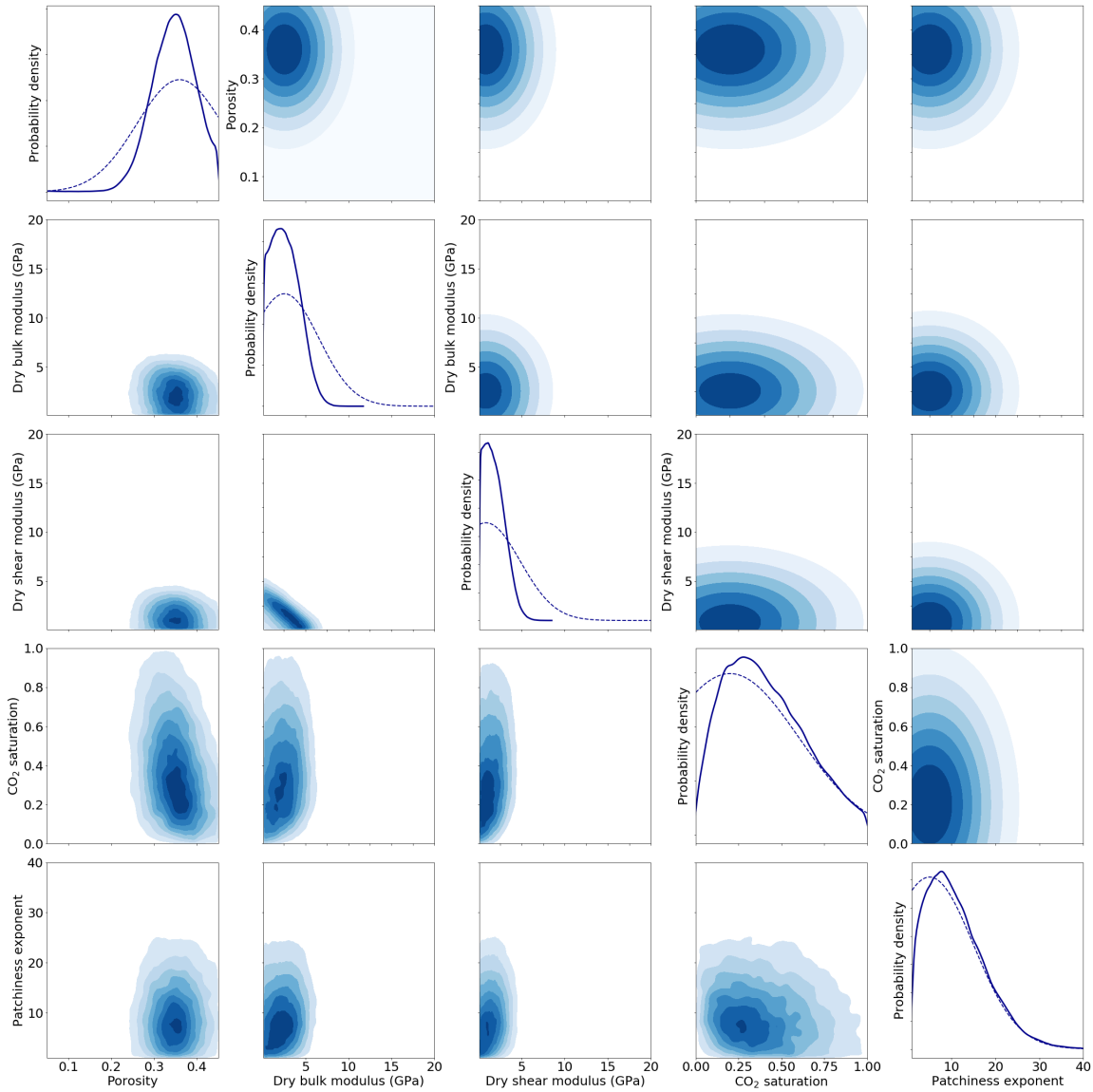

Figure 7: Monitor case - Gaussian prior information and some parameters fixed - Input data = V_P, ρ - $S_{CO_2} = 20\%$.
Bayesian rock physics inversion results after search and appraisal stages. The upper right half gives the 2D prior distributions (normal distributions with properties given in Table 3), while the diagonal gives the 1D marginal posterior PDFs in continuous blue lines and the 1D prior distribution in dashed blue lines, and the lower left half gives the 2D marginal posterior PDFs. Posterior marginal distributions are calculated with kernel density estimates. The results are given for the monitor case where five rock physics parameters are inverted. The input data are P-wave velocity V_P and bulk density ρ. The prior distributions are given for porosity, dry bulk and shear moduli, saturation and patchiness exponent. The other parameters (K_S, ρ_S, K_w, ρ_w, K_{CO_2} and ρ_{CO_2}) are fixed to their true values. The CO_2 saturation is equal to 20 %.

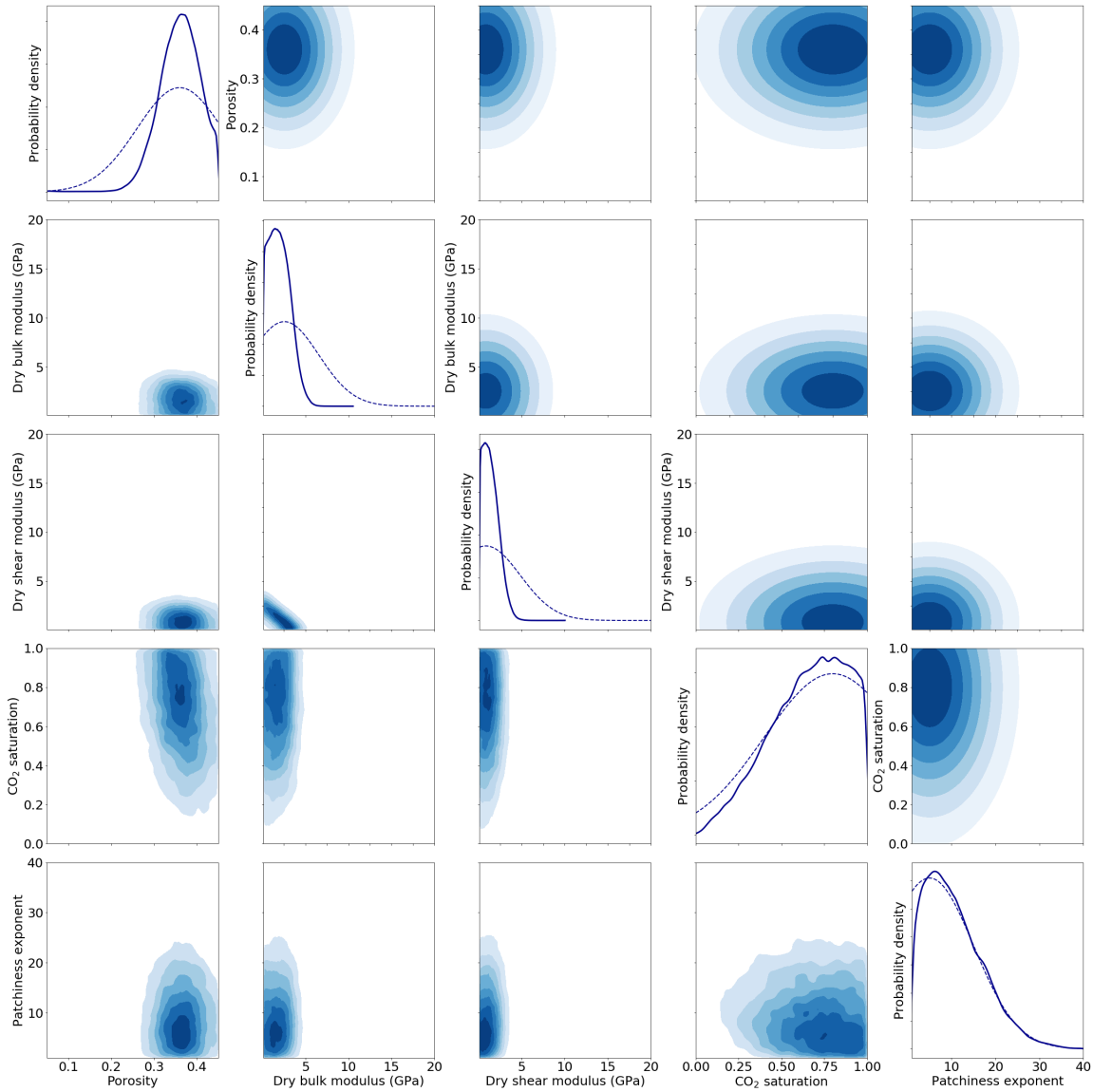

Figure 8: Monitor case - Gaussian prior information and some parameters fixed - Input data = V_P, ρ - $S_{CO_2} = 80\%$.
Bayesian rock physics inversion results after search and appraisal stages. The upper right half gives the 2D prior distributions (normal distributions with properties given in Table 3), while the diagonal gives the 1D marginal posterior PDFs in continuous blue lines and the 1D prior distribution in dashed blue lines, and the lower left half gives the 2D marginal posterior PDFs. Posterior marginal distributions are calculated with kernel density estimates. The results are given for the monitor case where five rock physics parameters are inverted. The input data are P-wave velocity V_P and bulk density ρ. The prior distributions are given for porosity, dry bulk and shear moduli, saturation and patchiness exponent. The other parameters (K_S, ρ_S, K_w, ρ_w, K_{CO_2} and ρ_{CO_2}) are fixed to their true values. The CO_2 saturation is equal to 80 %.

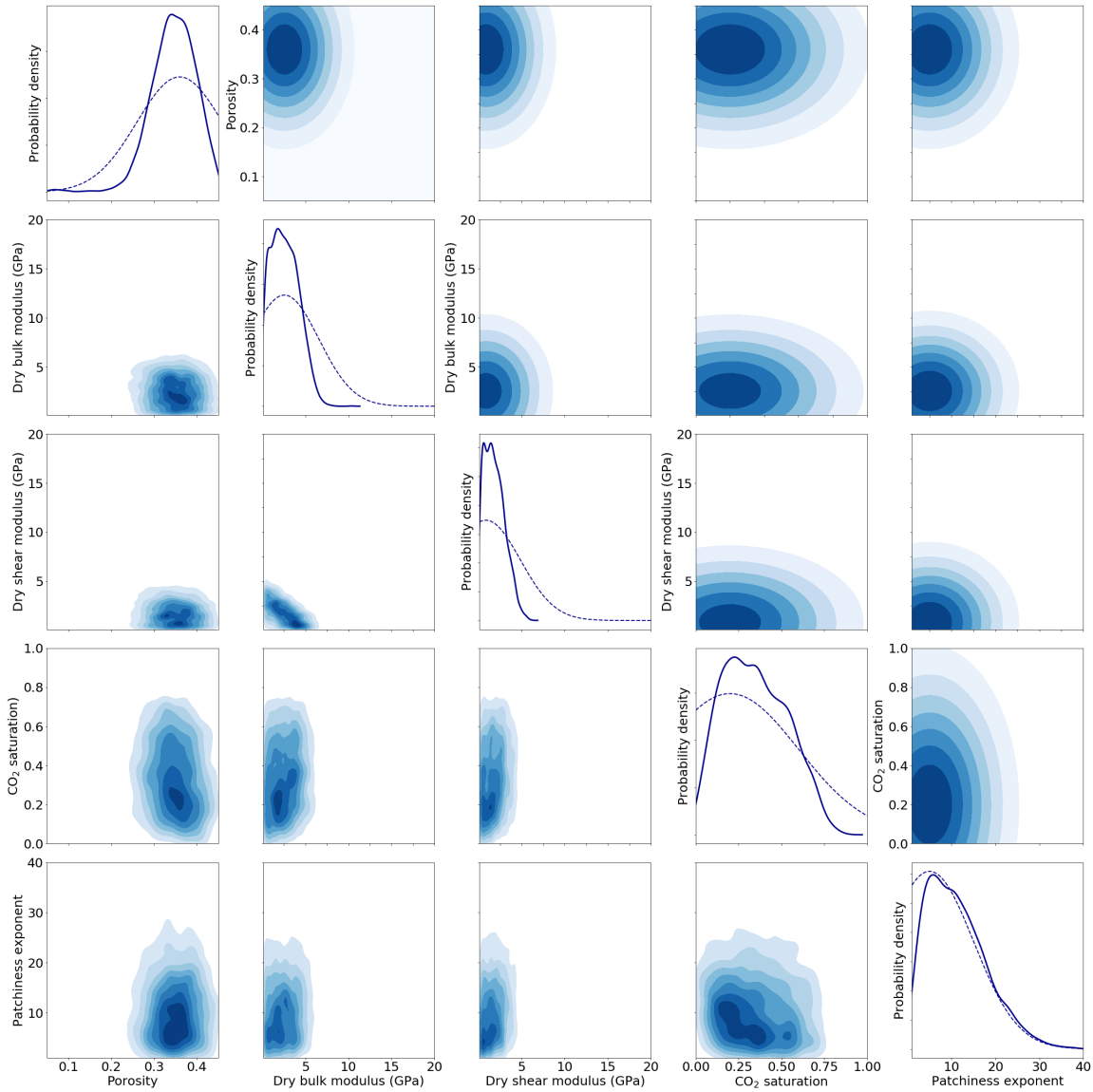

Figure 9: Monitor case - Gaussian prior information and some parameters fixed - Input data = V_P, ρ, R_t - $S_{CO_2} = 20\%$.
Bayesian rock physics inversion results after search and appraisal stages. The upper right half gives the 2D prior distributions (normal distributions with properties given in Table 3), while the diagonal gives the 1D marginal posterior PDFs in continuous blue lines and the 1D prior distribution in dashed blue lines, and the lower left half gives the 2D marginal posterior PDFs. Posterior marginal distributions are calculated with kernel density estimates. The results are given for the monitor case where five rock physics parameters are inverted. The input data are P-wave velocity V_P, bulk density ρ and resistivity R_t. The prior distributions are given for porosity, dry bulk and shear moduli, saturation and patchiness exponent. The other parameters (K_S, ρ_S, K_w, ρ_w, K_{CO_2}, ρ_{CO_2}, σ_w, m and n) are fixed to their true values. The CO_2 saturation is equal to 20 %.

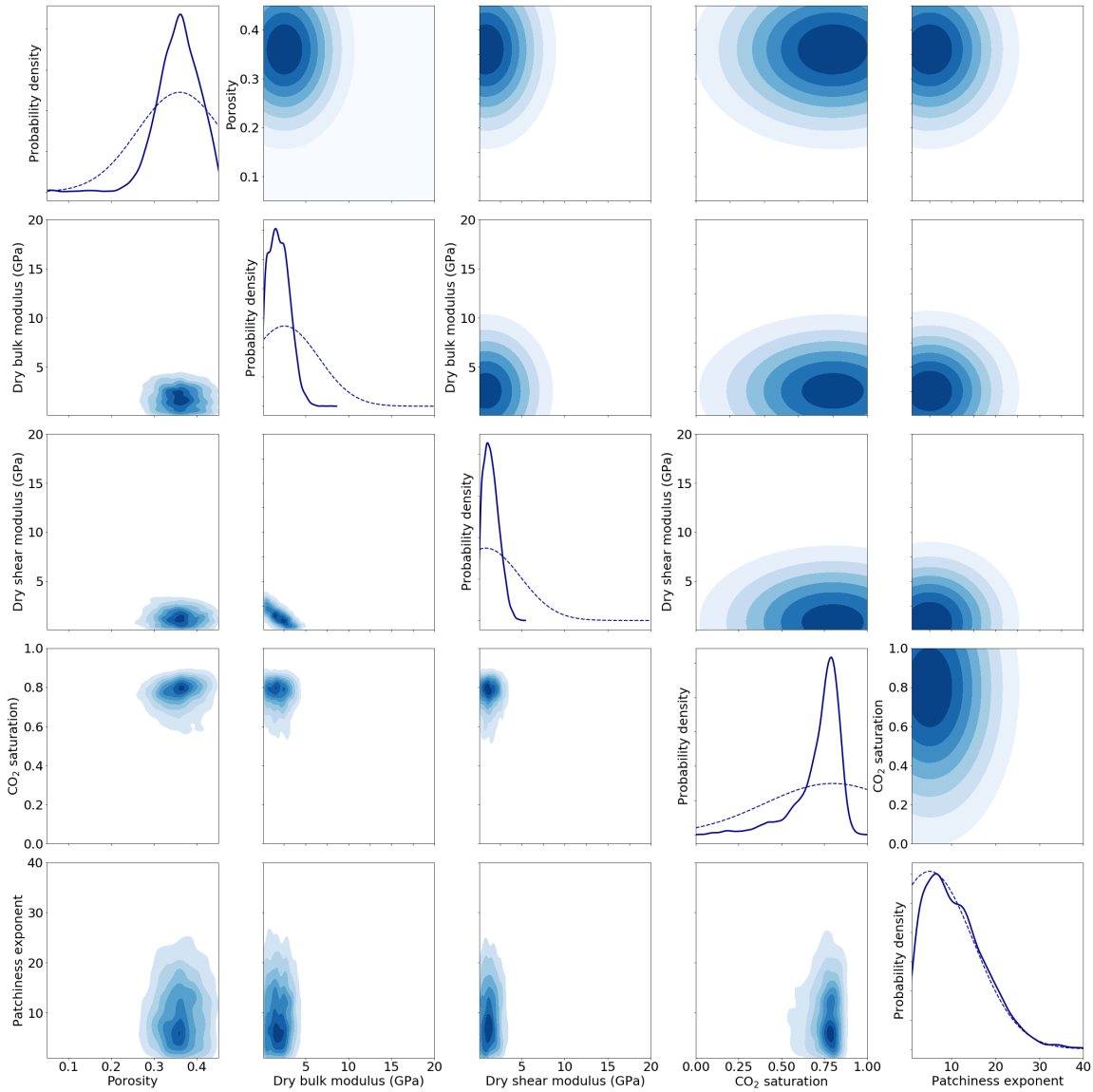

Figure 10: Monitor case - Gaussian prior information and some parameters fixed - Input data = V_P, ρ, R_t - $S_{CO_2} = 80\%$.
Bayesian rock physics inversion results after search and appraisal stages. The upper right half gives the 2D prior distributions (normal distributions with properties given in Table 3), while the diagonal gives the 1D marginal posterior PDFs in continuous blue lines and the 1D prior distribution in dashed blue lines, and the lower left half gives the 2D marginal posterior PDFs. Posterior marginal distributions are calculated with kernel density estimates. The results are given for the monitor case where five rock physics parameters are inverted. The input data are P-wave velocity V_P, bulk density ρ and resistivity R_t. The prior distributions are given for porosity, dry bulk and shear moduli, saturation and patchiness exponent. The other parameters (K_S, ρ_S, K_w, ρ_w, K_{CO_2}, ρ_{CO_2}, σ_w, m and n) are fixed to their true values. The CO_2 saturation is equal to 80 %.

REAL DATA CASE STUDY: SLEIPNER CO_2 STORAGE MONITORING

Seismic and CSEM inversion results

Following the sensitivity tests of the previous section, we choose an appropriate strategy for estimating relevant properties from Sleipner data. Before CO_2 injection, we use seismic 1994 vintage data to derive P-wave velocity and bulk density models (Yan et al., 2019). Along the same 2D inline (inline 1836), we use the 2008 seismic vintage to derive P-wave velocity and bulk density models showing a strong velocity drop due to the injected CO_2 (Romdhane and Querendez, 2014). In addition, 2D CSEM data were acquired in 2008 and CSEM inversion is carried out by Park et al. (2013) and Bøe et al. (2017) to derive resistivity models. The chosen seismic 2D line (inline 1836) intersects the injection point and the CSEM line in the southern part of the CO_2 plume (Figure 11). We extract the corresponding 1D P-wave velocity, density and resistivity profiles at this location. Extracted 1D profile of P-wave velocity for baseline and monitor, of density (for baseline) and resistivity (for monitor) are displayed in Figure 12 along with uncertainty ranges for these input data. It is worth noting the strong decrease of P-wave velocity between monitor and baseline cases from 850 m deep and the high resistivity values for the same depth range.

Rock physics model calibration

As described in the rock physics model section and displayed in the sensitivity tests, there is a trade off between CO_2 saturation and patchiness exponent. This exponent describes the way the fluid phases are mixed in the pore space and allow to build an effective fluid bulk modulus K_f. Using the parameters given in Table 3 for the typical monitor case, we

derive the values of P-wave velocity and resistivity with respect to CO_2 saturation in Figure 13. We observe large differences of the P-wave velocity response depending on the value of the patchiness exponent e. When e is close to 40, the velocity drop is very sharp and the velocity change is small when CO_2 saturation is greater than 0.2. This corresponds to fluid mixing so-called uniform mixing, i.e., that both fluid phases (supercritical CO_2 and brine) are mixed at the finest scale. When the patchiness exponent decrease towards 1, we tend towards an almost linear change of P-wave velocity versus saturation. The extreme case of $e = 1$ corresponds to so-called patchy mixing. Consequently, the quantitative interpretation of a velocity change requires the estimation of the patchiness exponent. Full calibration of the Biot-Gassmann rock physics model for Sleipner Utsira reservoir is carried out by Dupuy et al. (2017).

The resistivity response to the changes of saturation is driven by the Archie law (see rock physics models section) and depends on two empirical coefficients. We observe a large change in resistivity for CO_2 saturations greater than 0.8. The resistivity anomaly derived from CSEM inversion stays however below 10 Ω.m (Figure 12). The saturation exponent is commonly set to 2 (Carrigan et al., 2013; Falcon-Suarez et al., 2017) and the cementation exponent is related to pore tortuosity and evaluated between 1.0 and 1.5 in clean sands (Pride, 2005). It is worth noting that the well-known fizz gas effect (weak sensitivity of V_P to change of saturation when $S_{CO_2} > 0.5$) is counterbalanced by the better sensitivity of resistivity to these high CO_2 saturations. In addition to making the inverse system less under-determined, it is one of the main reasons for combining seismic and EM input data, i.e., to have a better constraints on the whole range of saturations.

Baseline results

Rock frame properties are inverted with baseline seismic data along the 1D profile (Figure 14). The inversions are carried out independently for each depth point and there is no additional constraint on spatial correlation than those inherent to the data itself. The grains and fluid parameters are also inverted (but not displayed here) and constrained using prior information defined in Table 2. We give the 1D profile of rock frame parameters (porosity, dry bulk and shear moduli) with confidence intervals in the reservoir target where CO_2 will be injected. As expected, the Utsira sandstone shows very good reservoir quality with high porosity and low dry bulk and shear moduli. We can observe a decrease of porosity ϕ (and associated increase of K_D and G_D) between 900 m and 950 m deep, which can be interpreted as the presence of thin interbedded shale layers.

Monitor results

In a second step, using 2008 monitor data (P-wave velocity, bulk density and resistivity), we estimate CO_2 saturation and patchiness exponent (Figure 15), and we update porosity, dry bulk and shear moduli distributions. Posterior PDFs of rock frame, grains and fluid parameters obtained in the baseline tests are used as prior distributions in the monitor case and 99% confidence intervals are extracted from the baseline posterior PDF to define inversion limits in the monitor case (i.e., limits of the model space).

We showed in the sensitivity study above that combining resistivity and seismic data (P-wave velocity and density) is crucial for obtaining correct estimates of CO_2 saturations, especially when the CO_2 saturation is large. The CO_2 saturation profile shows good constraints with high saturation at the top of the reservoir while the patchiness exponent has

a large uncertainty, in agreement with sensitivity tests. It is worth noting that the resolution of the depth profile for the saturation is quite low compared to expected results from time-lapse seismic or seismic inversions at Sleipner (Dupuy et al., 2017). In this case, the resistivity is the main driver of the saturation estimates and the spatial resolution of CSEM inversion is inherently lower than seismic inversion (Dell'Aversana, 2014). But, joint inversion of resistivity and P-wave velocity is the only way to mitigate uncertainties around patchiness exponent, i.e., the way the CO_2 and brine phases are mixed in the pore space (Subagjo et al., 2018). Gravimetry data can also be used for similar purposes and included in a joint inversion workflow, but the resolution and time-lapse limitations should be handled with care (Landrø and Zumberge, 2017).

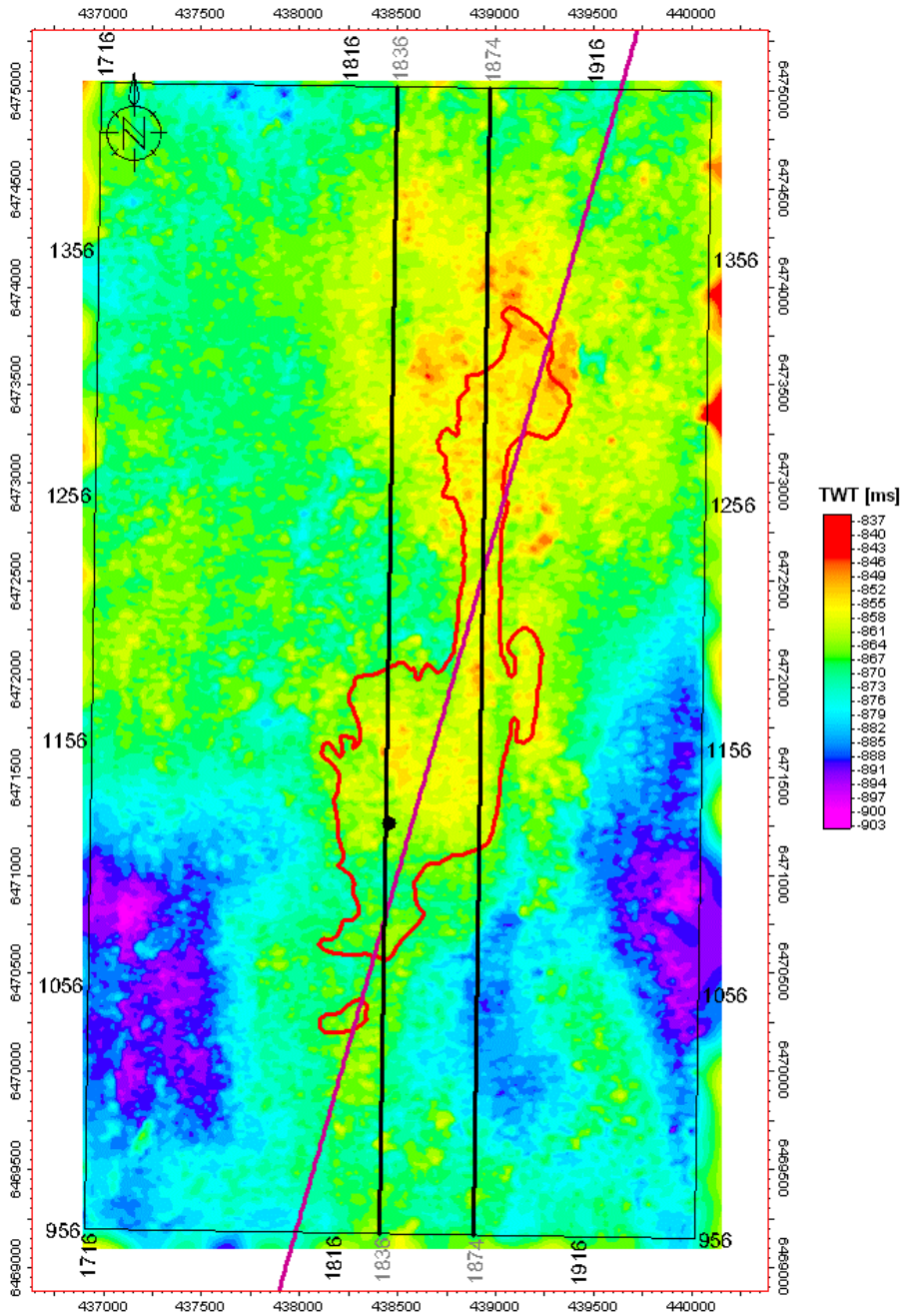

Figure 11: Location map of Sleipner CSEM and seismic lines. The black dot is the projection of the injection point. The color background give the depth of the interpreted Utsira reservoir top (Two Way Travetime, TWT) on the seismic 3D cube. The red area is the interpreted CO_2 plume extension in the top layer in 2008. The western North-South black line is the selected seismic 2D inline 1836 used for FWI data. The purple line (SW to NE) is the CSEM 2D line. We use the 1D profiles of resistivity and P-wave velocity derived from CSEM inversion and FWI and extracted where the seismic inline 1836 (western black line) and the CSEM line are crossing, i.e., in the southern part of the CO_2 plume.

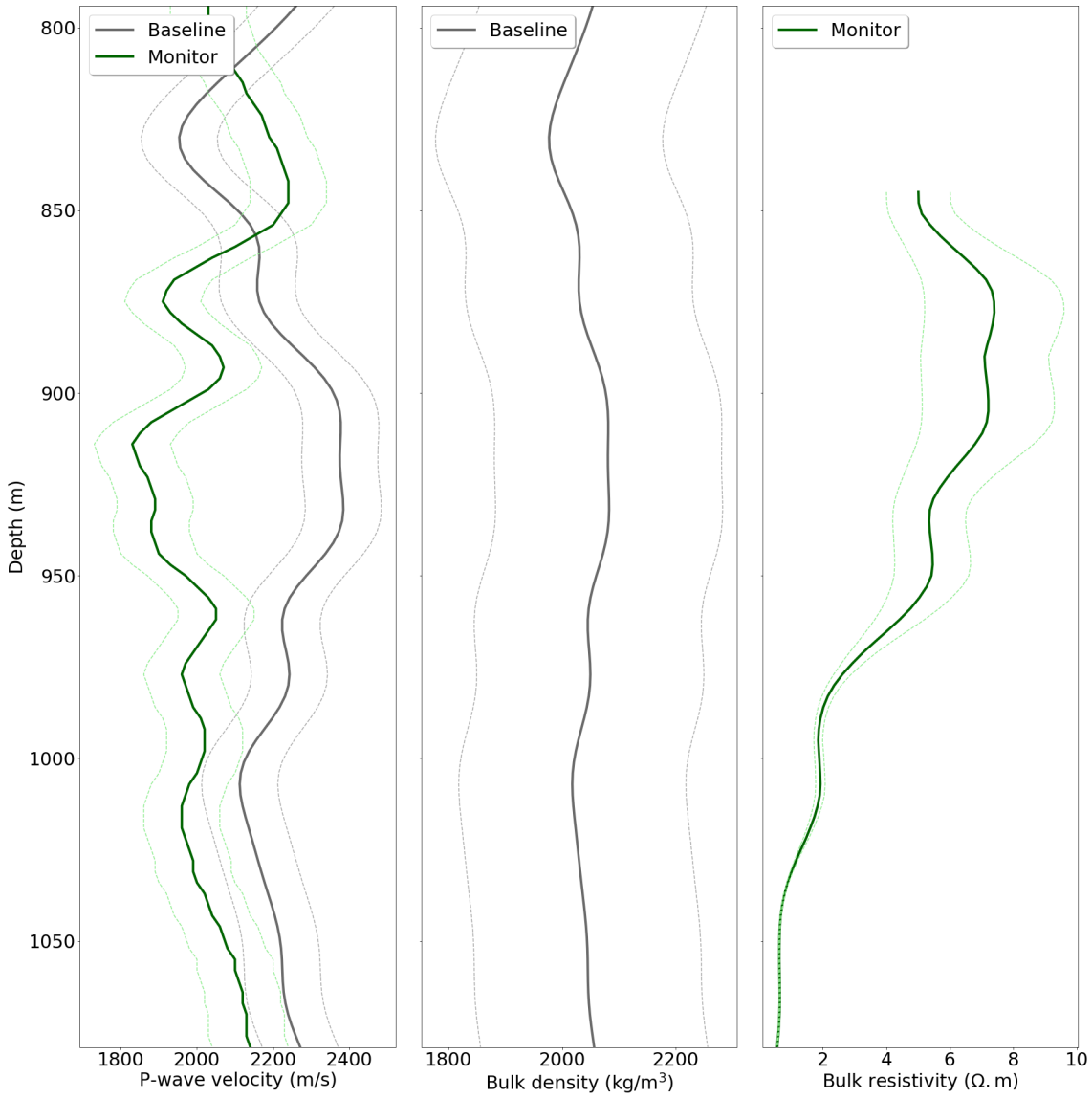

Figure 12: 1D depth profiles of P-wave velocity V_P (left), bulk density ρ (middle) and bulk resistivity R_t (right) extracted where seismic inline 1836 and CSEM inline are crossing (see Figure 11). The continuous lines stand for the values obtained by FWI and CSEM inversion while the dashed lines give the uncertainty range estimated in the inversions and propagated in the rock physics inversion step through the data covariance matrix $\boldsymbol{C_d}$. The grey lines are the data extracted for the baseline case (1994 vintage) while the green lines are the data extracted for the monitor case (2008 vintage).

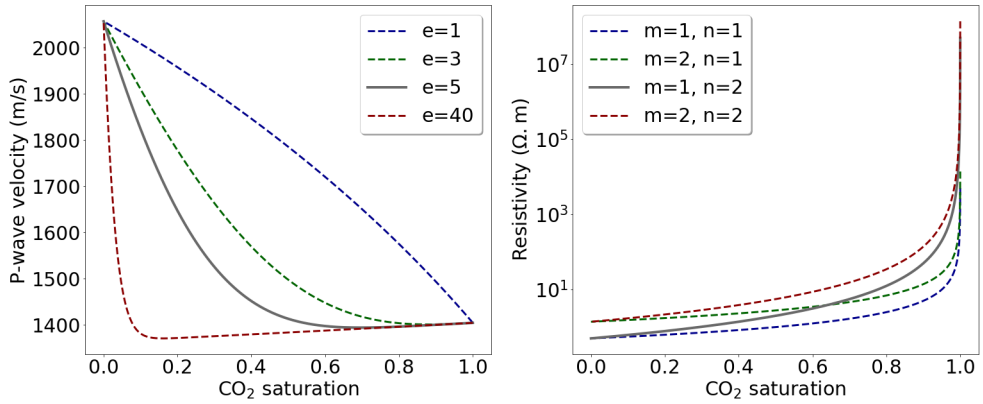

Figure 13: P-wave velocity V_P (left) and resistivity R_t (right) with respect to CO_2 saturation. The P-wave velocity is calculated with different values of patchiness exponent e (1 in blue dashed line, 3 in green dashed line, 5 in continuous grey line and 40 in red dashed line). The resistivity is calculated for different combinations of cementation exponent m and saturation exponent n ($m = 1$ and $n = 1$ in blue dashed line, $m = 2$ and $n = 1$ in green dashed line, $m = 1$ and $n = 2$ in grey continuous line and $m = 2$ and $n = 2$ in red dashed line). Note that the grey lines ($e = 5$ for P-wave velocity and $m = 1$ and $n = 2$ for resistivity) are the values chosen in the sensitivity tests.

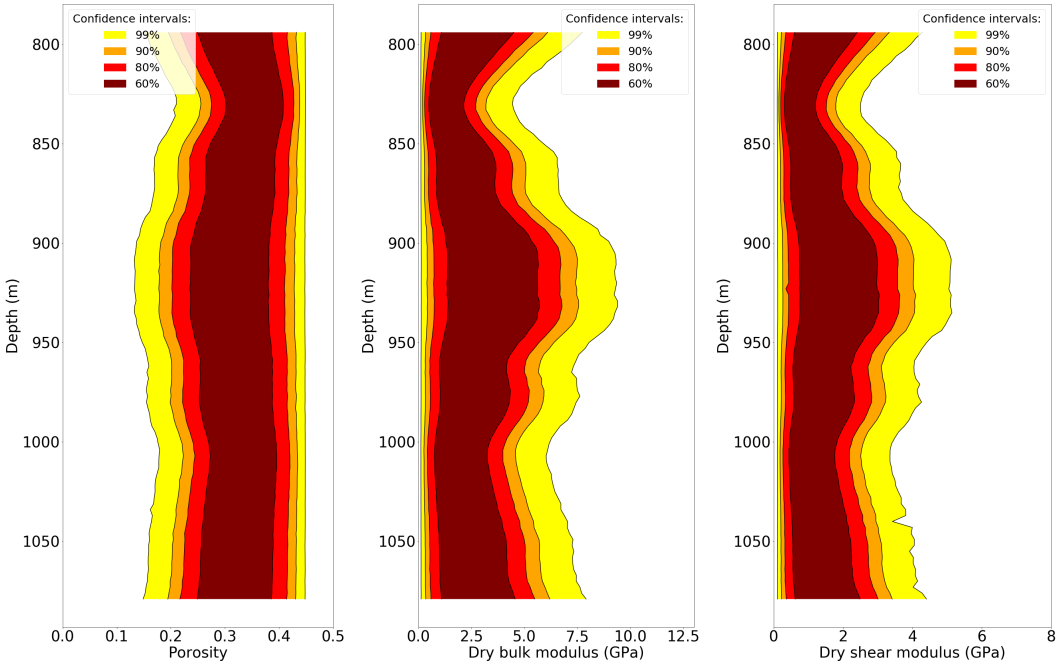

Figure 14: Bayesian rock physics inversion results for the 1D Sleipner profile (crossing point between seismic inline 1836 and CSEM line). Baseline case with P-wave velocity and bulk density seismic input data derived by FWI. From left to right, the confidence intervals for porosity, dry bulk and shear moduli are given versus depth.

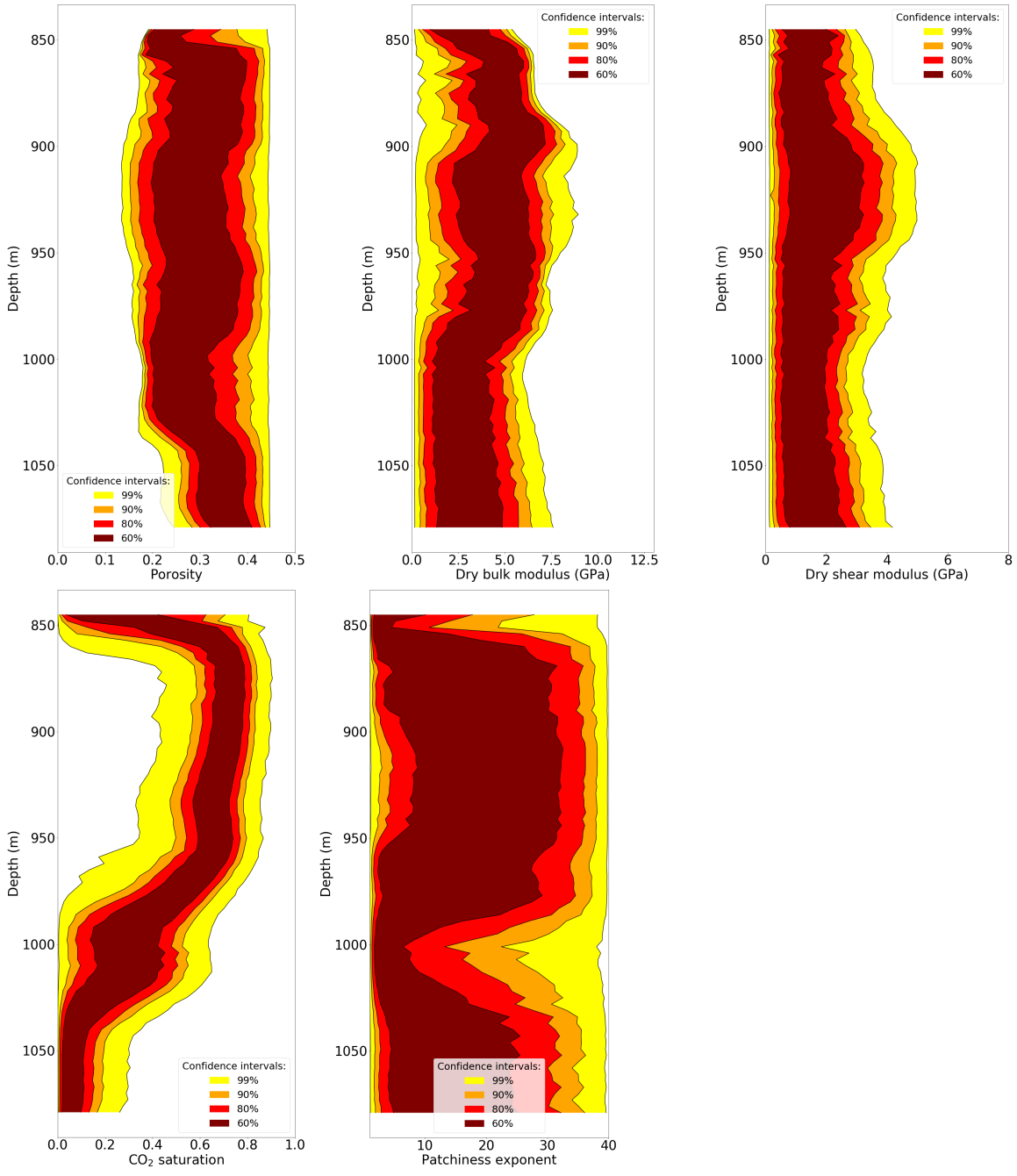

Figure 15: Bayesian rock physics inversion results for the 1D Sleipner profile (intersection between seismic inline 1836 and CSEM line). Monitor case with P-wave velocity and bulk density (from seismic FWI) and resistivity (from CSEM inversion) input data. Confidence intervals versus depth for porosity (top left), dry bulk (top middle) and shear (top right) moduli, CO_2 saturation (bottom left) and patchiness exponent (bottom middle). Prior distributions from baseline inversion results are used for rock frame properties (Figure 14).

DISCUSSIONS

One of the main limitations of Bayesian inversion is the computational burden. Table 4 summarizes the requirements for the search and appraisal stages of the different cases. When the complexity of the forward model increases, along with the number of dimensions in the model space, obtaining a sufficient number of resampled models is time consuming. Code parallelization is an obvious direction to mitigate such numerical limitations given that the random walks are independent.

In all our tests, we have included noise statistics assuming that the data covariance matrix is diagonal. We use a standard deviation equal to 100 m/s for V_P, 100 kg/m^3 for ρ (and 200 kg/m^3 for the 1D real data case) and 5 Ω.m for R_t. Correlations between these data uncertainties would be interesting to consider. In many cases, the density is derived from P-wave velocity using an empirical law or velocity and density can also be estimated from the same geophysical inversion technique as uncorrelated data variables.

We have mainly shown results of 1D and 2D marginal distributions but other Bayesian indicators can be derived and analyzed like the posterior covariance matrix, the correlation matrix or the resolution matrix. It is also worth noting that we use the appraisal stage as a "correction" procedure to get more reliable uncertainty evaluation as the ensemble derived in the search stage is already distributed according to a given PDF. The appraisal stage allows to get statistically meaningful indicators and ensure that the model space has been well explored (Sambridge, 1999b). The principle of Bayesian inference (Tarantola, 2005) is that all models bring relevant information to understand the inverse problem and the appraisal or sampling stage is needed to reliably approximate the posterior PDF.

For the 1D real data case, the inversions are run point-wise, i.e., there is no depth

(spatial) correlation between parameters. Lithological knowledge and information from e.g., log data or structural interpretation, should be considered to build a more realistic prior model. Such spatial consistency problems are discussed by Dupuy et al. (2016b).

Suitable definition of prior distribution is also critical in Bayesian inversions (Tarantola, 2005). We use uniform and normal distributions, while Gaussian mixtures (Fjeldstad and Grana, 2018) or other distributions may be considered since the proposed approach is not linearized and is rather generic. This is one of the main novelties of our approach.

All of our sensitivity tests are designed to determine what is the optimal parametrization (input data, inverted parameters, a priori models) for the real data case of Sleipner where the available data is limited i.e., one 2D CSEM line (2008 vintage) and 3D seismic data from 1994 and 2008. We have chosen to run acoustic FWI for the seismic data, so we are limited to estimate P-wave velocity and density with FWI, while we get horizontal and vertical resistivity from the CSEM inversion (only for the monitor case). Elastic FWI (and thus estimates of shear-wave velocity) is not carried out for several reasons: (1) the seismic data are recorded with conventional streamer acquisition (pressure from hydrophones), so it is challenging to infer shear wave velocity, (2) the offset range is limited to 1800 m and the shear-wave conversions are consequently limited, (3) the data quality is very different between 1994 and 2008 vintages.

Estimating shear-wave velocity would require AVO inversion, which is possible and has been done at Sleipner (Jullum and Kolbjørnsen, 2016; Haffinger et al., 2016), but joint inversion with CSEM data on the side of the plume (where CSEM and seismic lines are crossing) would be difficult. S-wave velocity model is useful for better estimating density, which is not updated in our acoustic FWI approach but correlated to the P-wave velocity

with empirical relations. It is a well-known problem that the density is difficult to assess in seismic inversion and especially with FWI. We have tested synthetic rock physics inversion with S-wave velocity as additional input (to P-wave velocity and density), and observe that the probability density peaks are slightly higher for rock frame properties (K_D, G_D and especially ϕ) when V_S is used but the "fluid" properties (S_{CO_2}, e) are not improved.

Finally, one of the main limitations is related to the forward rock physics models themselves. Models used in our approach are fairly simple compared to recent advances in the rock physics field. There is a wide range of models describing in detail (experimentally and theoretically) different effects occurring when seismic waves are travelling through a partially saturated medium, including pressure effects, opening and closing of micro-cracks, or fluid effects due to patchy saturation. These "advanced" rock physics models are very relevant but there are several good reasons explaining the choice of simple rock physics models in our work (Gassmann equations with effective fluid phase).

First, the rock physics inverse system is highly under-determined (more parameters to invert than available data). Usually, only one to three data types are available (P-wave velocity, maybe density, S-wave velocity or resistivity) and there is a minimum of seven parameters to estimate/invert in the best case (if only one fluid, baseline case). Even in this simplest case, we demonstrate that strong a priori information is required in order to converge towards the correct estimation of these parameters. If there are two fluid phases in the pores, the model space has 11 parameters to estimate and still a limited number of input data. Using more complex rock physics models usually implies dealing with a higher number of parameters (e.g., crack aspect ratio, crack density, patches size, various empirical constants). The proper exploration and sampling of high dimensional space and the numerical cost can become prohibitively high to get a good sampling (well-known "curse

of dimensionality" problem).

Second, pore pressure effects are negligible at Sleipner due to the size of the aquifer (Chadwick et al., 2012), so the observed P-wave velocity change is only affected by the change in fluid saturation. Consequently, considering rock physics models where pore pressure is explicit is not useful for Sleipner data. However, our inversion approach is able to handle different rock physics models, including those where pore pressure effects are explicit (Hertz-Mindlin model, Walton model, pore space stiffness model or crack models).

Third, wave induced fluid flow (WIFF) models or fluid effects due to patchy distribution of the fluid phases in the pore space are relevant to consider at Sleipner as the Utsira reservoir is a high porosity/high permeability sandstone saturated with two fluids (brine and supercritical CO_2) of different mobility (Rubino et al., 2011). However, if the attenuation is better described at seismic frequencies by WIFF models, seismic velocities are mostly affected at higher frequencies and Gassmann relations are consequently considered as a good approximation at seismic frequencies (Rasolofosaon and Zinszner, 2007). Rock physics inversion tests using patchy saturation models (White, 1975; Dutta and Odé, 1979; Pride et al., 2004) are run by Dupuy et al. (2016c) and the conclusion is that simpler partial saturation models as effective fluid phase perform better than complex patchy saturation models due to a lower number of parameters.

In addition, neither the rock physics models nor seismic and EM wave propagation will be able to describe accurately the physics in the porous media. If we consider other monitoring sites, pore pressure changes might be crucial to take into account due to their competitive effects with CO_2 saturation on the seismic response (Hansen et al., 2013). One way to mitigate the uncertainty in the rock physics modeling is to make the model itself as

a degree of freedom in the system but this is out of the scope of this work and would require heavy calibration and classification techniques with extensive well log and laboratory data (Johansen et al., 2013).

Table 4: Number of models generated for the NA search and appraisal stages for the different cases. n_{samp}, n_{cell}, n_{iter} and m_{min} are the number of samples at each iteration, the number of resampled cells, the number of iterations during the search stage and the minimum misfit reached during the search stage, respectively. n_{walks}, n_{steps} and n_{models} are the number of independent walks, the number of steps/iterations, and the total number of resampled models during the appraisal stage. The total number of models depends on n_{walks} and n_{steps}, but also on the convergence rate defined by the potential scale reduction factor (Sambridge, 1999b). For the 1D real data cases, we do not give any total number of resampled models as there is 79 independent inversions (79 depth samples), so n_{models} might be different for each depth, depending on the convergence rate.

Test case	Search stage				Appraisal stage		
	n_{samp}	n_{cell}	n_{iter}	m_{min}	n_{walks}	n_{steps}	n_{models}
Baseline, uniform prior, Figure 3	300	300	100	$1.00\ 10^{-6}$	10 000	80	800 000
Baseline, prior, Figure 4	300	300	100	$7.33\ 10^{-5}$	10 000	80	800 000
Monitor, uniform prior, Figure 5	300	300	100	$2.10\ 10^{-6}$	10 000	80	800 000
Monitor, Gaussian prior, Figure 6	300	300	100	0.079	10 000	80	800 000
Monitor, parameters fixed, $S_{CO_2} = 0.2$, Figure 7	1 000	1 000	50	$1.84\ 10^{-5}$	10 000	80	1 600 000
Monitor, parameters fixed, $S_{CO_2} = 0.8$, Figure 8	1 000	1 000	50	$2.52\ 10^{-5}$	10 000	80	1 600 000
Monitor, input data: V_P, ρ, R_t, $S_{CO_2} = 0.2$, Figure 9	1 000	1 000	50	$4.40\ 10^{-5}$	50	80	1 000 000
Monitor, input data: V_P, ρ, R_t, $S_{CO_2} = 0.8$, Figure 10	1 000	1 000	50	$2.01\ 10^{-5}$	50	80	1 000 000
Sleipner 1D, baseline, Figure 14	1 000	1 000	10	Variable	100	40	Variable
Sleipner 1D, monitor, Figure 15	1 000	1 000	10	Variable	100	40	Variable

CONCLUSIONS

We demonstrate a non-linearized Bayesian rock physics inversion method which is able to handle non-Gaussian model properties behaviour. The search and importance sampling stages are implemented to quantify uncertainty in the rock physics parameters estimation. The sensitivity tests show that we can estimate rock frame parameters and porosity with a good confidence before the CO_2 injection, thanks to the limited size of the model space (brine saturated porous medium). When partial saturations in brine and CO_2 are present,

it is necessary to add strong prior information from the baseline inversion and fixed values for the less sensitive parameters. A good discrimination between CO_2 saturation and patchiness exponent (fluid distribution) is achieved by adding resistivity data (derived by CSEM inversion). This strategy is applied point-wise to 1D profiles extracted from real data at Sleipner. We obtain CO_2 saturation estimates that are consistent with geology structure, reservoir models and time-lapse seismic interpretations, with a quantified uncertainty while the patchiness exponent is more loosely constrained.

REFERENCES

Abubakar, A., G. Gao, T. Habashy, and J. Liu, 2012, Joint inversion approaches for geophysical electromagnetic and elastic full-waveform data: Inverse Problems, **28**, 055016.

Aragao, O. and P. Sava, 2020, Elastic full-waveform inversion with probabilistic petrophysical model constraints: Geophysics, **85(2)**, R101–R111.

Archie, G. E., 1942, The electrical resistivity log as an aid in determining some reservoir characteristics: Transactions of the American Institute of Mining and Metallurgical Engineers, **146**, 55–62.

Avseth, P., T. Mukerji, and G. Mavko, 2005, Quantitative seismic interpretation: Applying rock physics tools to reduce interpretation risk: Cambridge University Press.

Batzle, M. and Z. Wang, 1992, Seismic properties of pore fluids: Geophysics, **57**, 1396–1408.

Bøe, L., J. Park, G. Sauvin, and M. Vöge, 2017, Improvement of resistivity imaging for an offshore CO_2 storage by filtering out seabed pipeline influence: Presented at the EAGE/SEG Research Workshop 2017.

Bosch, M., T. Mukerji, and E. F. Gonzalez, 2010, Seismic inversion for reservoir properties combining statistical rock physics and geostatistics: A review: Geophysics, **75**, 75A165–75A176.

Brie, A., F. Pampuri, A. Marsala, and O. Meazza, 1995, Shear sonic interpretation in gas-bearing sands: SPE Annual Technical Conf. 30595, 701–710.

Carrigan, C. R., X. Yang, D. J. LaBrecque, D. Larsen, D. Freeman, A. L. Ramirez, W. Daily, R. Aines, R. Newmark, J. Friedmann, and S. Hovorka, 2013, Electrical resistance tomographic monitoring of CO_2 movement in deep geologic reservoirs: International Journal of Greenhouse Gas Control, **18**, 401–408.

Ceci, F., M. Clementi, I. Guerra, and M. Mantovani, 2014, Integrated interpretation and

simultaneous joint inversion of CSEM and seismic datasets-the sunshine case: 76th EAGE Conference and Exhibition 2014, 1–5.

Chadwick, R., G. Williams, J. Williams, and D. Noy, 2012, Measuring pressure performance of a large saline aquifer during industrial-scale CO_2 injection: The Utsira Sand, Norwegian North Sea: International Journal of Greenhouse Gas Control, **10**, 374 – 388.

Chadwick, R., P. Zweigel, U. Gregersen, G. Kirby, S. Holloway, and P. Johannessen, 2004, Geological reservoir characterization of a CO_2 storage site: The Utsira Sand, Sleipner, northern North Sea: Energy, **29**, 1371 – 1381.

Coléou, T., F. Allo, R. Bornard, J. Hamman, and D. Caldwell, 2005, Petrophysical seismic inversion, *in* SEG Technical Program Expanded Abstracts 2005, 1355–1358.

Colombo, D., G. McNeice, N. Raterman, M. Zinger, D. Rovetta, and E. S. Curiel, 2014, Exploration beyond seismic: The role of electromagnetics and gravity gradiometry in deep water subsalt plays of the Red Sea: Interpretation, **2(3)**, SH33–SH53.

Colombo, D. and D. Rovetta, 2018, Coupling strategies in multiparameter geophysical joint inversion: Geophysical Journal International, **215**, 1171–1184.

Colombo, D., D. Rovetta, and E. Turkoglu, 2018, Csem-regularized seismic velocity inversion: A multiscale, hierarchical workflow for subsalt imaging: Geophysics, **83(5)**, B241–B252.

de Figueiredo, L. P., D. Grana, M. Santos, W. Figueiredo, M. Roisenberg, and G. S. Neto, 2017, Bayesian seismic inversion based on rock-physics prior modeling for the joint estimation of acoustic impedance, porosity and lithofacies: Journal of Computational Physics, **336**, 128–142.

Dean, M. and O. Tucker, 2017, A risk-based framework for measurement, monitoring and verification (MMV) of the Goldeneye storage complex for the Peterhead CCS project,

UK: International Journal of Greenhouse Gas Control, **61**, 1–15.

Dell'Aversana, 2014, Integrated geophysical models: EAGE Publications.

Doyen, P., 2007, Seismic reservoir characterization: An earth modelling perspective, volume **2**: EAGE publications.

Du, Z. and L. M. MacGregor, 2010, Reservoir characterization from joint inversion of marine CSEM and seismic AVA data using Genetic Algorithms: a case study based on the Luva gas field, *in* SEG Technical Program Expanded Abstracts 2010, 737–741.

Duffet, C. and D. Sinoquet, 2006, Quantifying uncertainties on the solution model of seismic tomography: Inverse Problems, **22(2)**, 525.

Dupuy, B., A. Asnaashari, R. Brossier, S. Garambois, L. Metivier, A. Ribodetti, and J. Virieux, 2016a, A downscaling strategy from FWI to microscale reservoir properties from high-resolution images: The Leading Edge, **35**, 146–150.

Dupuy, B., S. Garambois, A. Asnaashari, H. M. Balhareth, M. Landrø, A. Stovas, and J. Virieux, 2016b, Estimation of rock physics properties from seismic attributes - Part 2: Applications: Geophysics, **81(4)**, M55–M69.

Dupuy, B., S. Garambois, and J. Virieux, 2016c, Estimation of rock physics properties from seismic attributes - Part 1: Strategy and sensitivity analysis: Geophysics, **81(3)**, M35–M53.

Dupuy, B., A. Romdhane, P. Eliasson, E. Querendez, H. Yan, V. A. Torres, and A. Ghaderi, 2017, Quantitative seismic characterization of CO_2 at the Sleipner storage site, North Sea: Interpretation, **5(4)**, SS23–SS42.

Dupuy, B., A. Romdhane, P. Eliasson, and H. Yan, 2021, Combined geophysical and rock physics workflow for quantitative CO_2 monitoring: International Journal of Greenhouse Gas Control, **In press**.

Dutta, A. J. and H. Odé, 1979, Attenuation and dispersion of compressional waves in fluid-filled porous rocks with partial gas saturation (White model)-Part I: Biot theory: Geophysics, **44**, 1777–1788.

Eliasson, P. and A. Romdhane, 2017, Uncertainty quantification in waveform-based imaging methods - a Sleipner CO_2 monitoring study: Energy Procedia, **114**, 3905–3915.

Eliasson, P., A. Romdhane, M. Jordan, and E. Querendez, 2014, A synthetic Sleipner study of CO_2 quantification using Controlled Source Electro-Magnetics and Full Waveform Inversion: Energy Procedia, **63**, 4249 – 4263.

Falcon-Suarez, I., H. Marín-Moreno, F. Browning, A. Lichtschlag, K. Robert, L. J. North, and A. I. Best, 2017, Experimental assessment of pore fluid distribution and geomechanical changes in saline sandstone reservoirs during and after CO_2 injection: International Journal of Greenhouse Gas Control, **63**, 356 – 369.

Falcon-Suarez, I., G. Papageorgiou, A. Chadwick, L. North, A. I. Best, and M. Chapman, 2018, CO_2-brine flow-through on an Utsira Sand core sample: Experimental and modelling. Implications for the Sleipner storage field: International Journal of Greenhouse Gas Control, **68**, 236–246.

Fjeldstad, T. and D. Grana, 2018, Joint probabilistic petrophysics-seismic inversion based on Gaussian mixture and Markov chain prior modelsProbabilistic petroelastic prediction: Geophysics, **83(1)**, R31–R42.

Gallardo, L. A. and M. A. Meju, 2007, Joint two-dimensional cross-gradient imaging of magnetotelluric and seismic traveltime data for structural and lithological classification: Geophysical Journal International, **169**, 1261–1272.

Gassmann, F., 1951, Über die elastizität poröser medien: Vierteljahrsschrift der Naturforschenden Gesellschaft in Zurich, **96**, 1–23.

Gelman, A., J. B. Carlin, H. S. Stern, D. B. Dunson, A. Vehtari, and D. B. Rubin, 2013, Bayesian data analysis: CRC press.

Ghaderi, A. and M. Landrø, 2009, Estimation of thickness and velocity changes of injected carbon dioxide layers from prestack time-lapse seismic data: Geophysics, **74(2)**, O17–O28.

Ghosh, R., M. K. Sen, and N. Vedanti, 2015, Quantitative interpretation of CO_2 plume from Sleipner (North Sea), using post-stack inversion and rock physics modeling: International Journal of Greenhouse Gas Control, **32**, 147–158.

Giraud, J., V. Ogarko, M. Lindsay, E. Pakyuz-Charrier, M. Jessell, and R. Martin, 2019, Sensitivity of constrained joint inversions to geological and petrophysical input data uncertainties with posterior geological analysis: Geophysical Journal International, **218**, 666–688.

Grana, D., T. Mukerji, J. Dvorkin, and G. Mavko, 2012, Stochastic inversion of facies from seismic data based on sequential simulations and probability perturbation method: Geophysics, **77(4)**, M53–M72.

Guéguen, Y. and V. Palciauskas, 1994, Introduction to the physics of rocks: Princeton University Press.

Gunning, J. and M. Glinsky, 2007, Detection of reservoir quality using Bayesian seismic inversion: Geophysics, **72(3)**, R37–R49.

Haffinger, P., F. Jedari Eyvazi, T. Steeghs, P. Doulgeris, and A. Gisolf, 2016, Quantitative prediction of injected CO_2 at Sleipner Using Wave-equation Based AVO: 78th EAGE Conference and Exhibition, 1–5.

Hansen, O., D. Gilding, B. Nazarian, B. Osdal, P. Ringrose, J.-B. Kristoffersen, O. Eiken, and H. Hansen, 2013, Snøhvit: the history of injecting and storing 1Mt CO_2 in the fluvial

Tubåen Fm: Energy Procedia, **37**, 35653567.

Hashin, Z. and S. Shtrikman, 1963, A variational approach to the elastic behavior of multiphase materials: Journal of the Mechanics and Physics of Solids, **11**, 127–140.

Hoversten, G. M., F. Cassassuce, E. Gasperikova, G. A. Newman, J. Chen, Y. Rubin, Z. Hou, and D. Vasco, 2006, Direct reservoir parameter estimation using joint inversion of marine seismic ava and csem data: Geophysics, **71(3)**, C1–C13.

Johansen, T. A., E. H. Jensen, G. Mavko, and J. Dvorkin, 2013, Inverse rock physics modeling for reservoir quality prediction: Geophysics, **78(2)**, M1–M18.

Jordan, M., D. Rippe, A. Romdhane, and C. Schmidt-Hattenberger, 2018, CO_2 monitoring at the Ketzin pilot site with joint inversion: Application to synthetic and real data: Fifth CO2 Geological Storage Workshop, European Association of Geoscientists, 1–5.

Jullum, M. and O. Kolbjørnsen, 2016, A Gaussian-based framework for local Bayesian inversion of geophysical data to rock properties: Geophysics, **81(3)**, R75–R87.

Landrø, M. and M. Zumberge, 2017, Estimating saturation and density changes caused by CO_2 injection at Sleipner using time-lapse seismic amplitude-variation-with-offset and time-lapse gravity: Interpretation, **5(2)**, T243–T257.

Lindeberg, E., 2013, Calculation of thermodynamic properties of CO_2, CH_4, H_2O and their mixtures also including salt with the Excel macro CO_2 Thermodynamics: SINTEF report.

Mavko, G., T. Mukerji, and J. Dvorkin, 2009, The rocks physics handbooks, tools for seismic analysis in porous media; second edition: Cambridge University Press.

Mosegaard, K. and A. Tarantola, 1995, Monte Carlo sampling of solutions to inverse problems: Journal of Geophysical Research, **100 B7**, 12431–12447.

Oh, S.-H. and B.-D. Kwon, 2001, Geostatistical approach to Bayesian inversion of geophysical data: Markov chain Monte Carlo method: Earth, planets and space, **53(8)**,

777–791.

Park, J., M. Fawad, I. Viken, E. Aker, and T. I. Bjørnarå, 2013, CSEM sensitivity study for Sleipner CO_2-injection monitoring: Energy Procedia, **37**, 4199 – 4206. GHGT-11.

Pawar, R. J., G. S. Bromhal, J. W. Carey, W. Foxall, A. Korre, P. S. Ringrose, O. Tucker, M. N. Watson, and J. A. White, 2015, Recent advances in risk assessment and risk management of geologic CO_2 storage: International Journal of Greenhouse Gas Control, **40**, 292–311.

Pride, S., 2005, Hydrogeophysics, chapter Relationships between seismic and hydrological properties, 253–284. Water Science and Technology Library, Springer.

Pride, S., J. Berryman, and J. Harris, 2004, Seismic attenuation due to wave-induced flow: Journal of Geophysical Research, **109**, 1–19.

Rasolofosaon, P. and B. Zinszner, 2007, The unreasonable success of Gassmann's theory... revisited: 12th international workshop on seismic anisotropy, Beijing, China.

Rippe, D., M. Jordan, A. Romdhane, C. Schmidt-Hattenberger, M. Macquet, and D. Lawton, 2018, Accurate CO_2 monitoring using quantitative joint inversion at the CaMI Field Research Station (FRS), Canada: Presented at the 14th International Conference on Greenhouse Gas Control Technologies-GHGT-14.

Romdhane, A. and E. Querendez, 2014, CO_2 characterization at the Sleipner field with full waveform inversion: application to synthetic and real data: Energy Procedia, **63**, 4358–4365.

Rubino, J. G., D. R. Velis, and M. D. Sacchi, 2011, Numerical analysis of wave-induced fluid flow effects on seismic data: Application to monitoring of CO_2 storage at the Sleipner field: Journal of Geophysical Research: Solid Earth, **116(B3)**.

Sambridge, M. and K. Mosegaard, 2002, Monte Carlo methods in geophysical inverse prob-

lems: Reviews of Geophysics, **40**, 1–29.

Sambridge, M. S., 1999a, Geophysical inversion with a neighbourhood algorithm - I. Searching a parameter space: Geophysical Journal International, **138**, 479–494.

———, 1999b, Geophysical inversion with a neighbourhood algorithm - II. Appraising the ensemble: Geophysical Journal International, **138**, 727–746.

Span, R. and W. Wagner, 1996, A new equation of state for carbon dioxide covering the fluid region from the triple-point temperature to 1100 K at pressures up to 800 MPa: Journal of physical and chemical reference data, **25**, 1509–1596.

Subagjo, I., B. Dupuy, J. Park, A. Romdhane, E. Querendez, and A. Stovas, 2018, Joint rock physics inversion of seismic and electromagnetic data for CO_2 monitoring at Sleipner: Presented at the 24th European Meeting of Environmental and Engineering Geophysics.

Tarantola, A., 2005, Inverse problem theory and methods for model parameter estimation: Society for Industrial and Applied Mathematics.

Thurin, J., R. Brossier, and L. Métivier, 2019, Uncertainty quantification with ensemble-based fwi-application to 2d obc data from the valhall field: Presented at the 81st EAGE Conference and Exhibition 2019.

Virieux, J. and S. Operto, 2009, An overview of full waveform inversion in exploration geophysics: Geophysics, **74(6)**, WCC1–WCC26.

White, J. E., 1975, Computed seismic speeds and attenuation in rocks with partial gas saturation: Geophysics, **40**, 224–232.

Yan, H., B. Dupuy, A. Romdhane, and B. Arntsen, 2019, CO_2 saturation estimates at Sleipner (North Sea) from seismic tomography and rock physics inversion: Geophysical Prospecting, **67**, 1055–1071.

Zhu, H., S. Li, S. Fomel, G. Stadler, and O. Ghattas, 2016, A Bayesian approach to estimate

uncertainty for full-waveform inversion using a priori information from depth migration: Geophysics, **81(5)**, R307–R323.